Guiding-center chaotic motion in three electrostatic waves

J. H. Misguich and R. Nakach
Association EURATOM-CEA, Département de Recherches sur la Fusion Contrôlée, Centre d'Etudes Nucléaires de Cadarache, 13108 Saint-Paul-lez-Durance CEDEX, France
(Received 26 December 1990)

The dynamics of guiding centers in a general configuration of three electrostatic plane waves is studied in the plane (x,y) perpendicular to a strong magnetic field. The associated Hamiltonian is nonautonomous with $1\frac{1}{2}$ degrees of freedom, and the conjugated variables are the coordinates (x,y). This is the simplest system that exhibits the onset of chaotic motion in electrostatic plasma turbulence. An explicit analytical solution is obtained for the unperturbed integrable system consisting of two low-amplitude waves, by solving a generalized Kepler equation. Chaotic diffusion of guiding centers becomes possible due to the existence of a third wave. As the amplitude of the perturbation increases, chaotic motion is first localized, then extended over a network spread over the whole phase space along separatrices, and finally densely covers the full space.

I. INTRODUCTION

In the community of plasma physicists, the most widely held view is that anomalous transport [1] over the main confinement region in a tokamak $[1 \leq q(r) \leq 2]$ is caused by the motion of electrons across the magnetic field, due to the $\mathbf{E}\times\mathbf{B}$ drift associated with low-frequency electrostatic turbulent fields [2]. These modes are characterized by frequencies ω much smaller than the gyrofrequencies Ω_i or Ω_e of the ions or electrons. When considering finite-amplitude waves, a complete approach of the electrostatic plasma turbulence problem would require a self-consistent treatment: the functional dependence of the electrostatic fields should be determined by and coupled to the nonlinear motion itself. This is justified namely by the fact that, with the anomalous transport, the stability of the drift modes depends on the nonlinear motion of the electrons, which may modify the electron charge-density response function [3,4].

Because of the extreme complexity of the self-consistent problem, theoretical and numerical studies have been undertaken for the simplified problem, considering particle diffusion in a given turbulent spectrum of electrostatic fluctuations [2,5]. Even in this case the nonlinear feature of the problem forces one to consider simplifying statistical assumptions in the theoretical study in order to make this problem tractable.

Another, even considerably more simplified, approach has been undertaken by Kleva and Drake [6] and Horton [7], who consider the stochastic $\mathbf{E}\times\mathbf{B}$ particle transport in two electrostatic waves, assuming that they depend only on two transverse dimensions. In these studies, the parallel motion is assumed to be decoupled from the perpendicular $\mathbf{E}\times\mathbf{B}$ drift motion, neglecting the shear effect of the magnetic field on the particle motion. The effect of a sheared magnetic field on the stochastic electron dynamics due to drift waves has been considered in Ref. [8].

However, a point, common to these studies, including a limited number of waves, is related to the description of the electrostatic waves. The potential associated with the waves is assumed to depend [by a product of trigonometric functions $\cos(k_x x)\cos(k_y y-\omega t)$] on the two coordinates x and y perpendicular to the magnetic field: it propagates generally in the y direction and is stationary in the x direction, corresponding to the radial equilibrium gradient direction of the plasma torus, due to its boundedness. This last hypothesis implies a mathematical structure of the potential which makes the guiding center motion already nonintegrable in the case of two waves of this kind (which actually amounts to four propagative plane waves).

In the approach we present here, we consider the motion of a guiding center in the potential of three electrostatic (plane) waves $\cos(\mathbf{k}_i\cdot\mathbf{r}-w_i t)$ which propagate both in the radial (x) and perpendicular-tangential (y) directions, with different wave-vector components. This is justified by the experimental observation that electrostatic turbulence seems to be isotropic in the plane perpendicular to the magnetic field [9,10]: one generally considers that, due to nonlinear coupling between the waves of the turbulent spectrum, there is an isotropization of the different waves in the two perpendicular directions.

Here we focus our attention on the mechanism responsible for the onset of stochastic motion in a restricted number of waves (picked, for instance, from a turbulent spectrum), and on the conditions for the existence of a chaotic threshold via numerical and analytical methods. This study was stimulated by a result obtained in previous numerical studies [5,11–15] in which an observed feature of the numerical models with many waves (typically 10^3) is the existence of a threshold in the value of the turbulent amplitude of the onset of chaos.

It is first shown that the two-dimensional guiding center motion, in the general case of two electrostatic waves, appears to be completely integrable. In this case the constancy of the Hamiltonian of this dynamical system takes the form of a generalized Kepler equation in

two variables. An angle-action-variables approach is explicitly given for the determination of the exact frequencies. In a modified phase space, invariant curves are obtained, which possibly exhibit resonances with elliptic points, provided that the amplitudes of the two electrostatic waves are sufficiently high. This "phase portrait" presents saddle connections between hyperbolic singular points at the separatrix. By adding a third wave of small amplitude, it is reasonable to expect that this structure will be destroyed, leading to a chaotic motion.

Indeed, in the case of three waves the time variable cannot be eliminated in general, and the motion is governed by a $1\frac{1}{2}$ degrees-of-freedom Hamiltonian. In the specific case of equal frequencies, with a particular class of orientations of the three wave vectors, it is possible to reduce the equations of motion to a unique time-dependent second-order differential equation in one variable. If moreover, the amplitudes are sufficiently large, this equation reduces to the well-known paradigm equation [16] corresponding to the motion of a charged particle in two electrostatic waves with no magnetic field. Numerous studies have shown the appearance of chaos in that system, with an analytical estimation of the threshold. Thus, at least in this limit, the guiding-center system in three waves is proved to be chaotic; the general case is studied numerically.

For low values of the amplitudes of the first two waves, we have derived an approximate description of the threshold of chaotic motion via the standard mechanism of resonance overlapping. For larger values of the amplitude of the third perturbation wave, we exhibit the mechanism leading to large-scale stochasticity in phase space, as the result of the collapse of two hyperbolic points, occurring when the amplitude of the perturbation reaches that of the two first waves. In the domain of large amplitude of the two first waves, a different mechanism is observed to yield large-scale stochasticity: the breaking of a resistant S-shaped curve, leading to a complex permeable structure, reminiscent of Cantori resulting from perturbation of Kolmogorov-Arnold-Moser (KAM) surfaces.

This paper is organized as follows. Section II is devoted to the analytical studies and Sec. III to the numerical simulations of guiding centers.

In Sec. II A we present the general equations of motion of a particle in three electrostatic low-frequency waves propagating in the plane perpendicular to a strong magnetic field, allowing a drift approximation, i.e., the equations of motion for the guiding centers. It is first shown that, in the unperturbed two-wave system, the time dependence can be eliminated in a reference frame moving at a resonant velocity with both frequencies, corresponding thus to an integrable system, as expected. In the three-wave system, the time dependence cannot be eliminated: the Hamiltonian has $1\frac{1}{2}$ degrees of freedom. The general equations of motion are given in Eqs. (11) and (12) in the form of evolution equations for the canonical phases ξ_1 and ξ_2 of the two first waves.

We introduce in Sec. II A the specific class of orientations of the three wave vectors, which will be considered in what follows. For this class, closed differential equations are derived for orthogonal phase coordinates $R=\xi_1-\xi_2$ and $S=\xi_1+\xi_2$, describing the "transverse" and "parallel" motion, respectively (with respect to the diagonal).

In Sec. II B we derive the explicit Chirikov criterion, obtained by perturbation of the analytical solution deduced for the two-wave problem. This analytical solution is derived in Sec. II B 1 in a parametric form, by solving a generalization of the Kepler equation in the "elliptic" (weak-amplitude) case. Angle and action variables are introduced in Sec. II B 2, and explicit expressions are obtained for the frequencies of the unperturbed trajectories. The Chirikov criterion is given in Sec. II B 3 in terms of the Fourier amplitudes $V_{m,n}$ of the perturbation.

The phase-space portrait of the unperturbed two-wave system is described in Sec. II C. For equal values and weak amplitude of the two waves (elliptic case), the general structure of the phase space is dominated by two straight lines and an S-shaped curve, which remain as the basic structure of the three-wave phase portrait. For larger amplitudes ("hyperbolic" case), stationary points appear in phase space and are calculated analytically.

In Sec. II D the general features of this phase portrait are used to derive an approximate solution for the two wave system, which is then perturbed in order to obtain an explicit expression of the Fourier amplitudes $V_{m,n}$ of the perturbation.

The equations of motion are solved numerically in Sec. III for a specific case of the wave-vector orientation class studied in Sec. II A. By perturbing the elliptic case, we observe in Sec. III A 1 the primary islands, the basic straight-line trajectories, and the S-shaped curve, in agreement with the corresponding analytical calculations presented. Other chains of primary resonances also appear for higher values of the amplitude, above threshold values predicted analytically.

When the amplitude of the perturbing wave reaches the value of the amplitude of the two basic waves, we have found [15,17] a very interesting phenomenon: *the collapse of two hyperbolic points* (Sec. III A 2), allowing a connection between the S-shaped curve and the straight lines, hence a stochastic feature of the trajectories also in the perpendicular direction. A first analytical study of this collapse is given in Sec. III A 3. Further work is in progress [18].

Beyond this collapse, a thin chaotic zone, extended in the whole space in both parallel and perpendicular directions, is obtained, forming a kind of "stochastic web" [19] along the regions of degeneracy of the unperturbed system, which are indeed the S-shaped curve and the straight line (Sec. III A 4). The threshold for complete stochasticity is obtained with a still larger perturbation. The observed zones of chaotic motion are explained in Sec. III A 5 in terms of island overlapping, in agreement with the analytical criterion.

In Sec. III B we study the onset of chaotic motion in the hyperbolic case. Here a different mechanism seems to be at the origin of large-scale stochasticity: before any collapse of hyperbolic points, the separating S-shaped curve is replaced by a permeable structure, allowing a chaotic diffusion in the whole phase space.

The conclusions of this comparison between simulations and analytical results are given in Sec. III C where the various phenomena observed in the onset of chaos are summarized (collapse, overlapping, subharmonic, stochastic web, permeable structure, etc.).

We report in Appendix A the comparison of the approximate frequencies (predicted by the approximate solution of the two-wave problem) with the exact ones. In Appendix B we report simulation results with different amplitudes of the two first waves: although the straight line is deformed, the topology of the phase-space portrait and the mechanisms leading to chaos are analogous.

II. GUIDING CENTER MOTION IN THREE WAVES

In the present work, we consider an electrostatic potential including three plane waves propagating in a plane $[\mathbf{r}=(x,y)]$:

$$\Phi(x,y,t)=\sum_{i=1}^{3} a_i \sin\xi_i(x,y,t) \tag{1}$$

with

$$\xi_i(x,y,t)\equiv k_i^x x+k_i^y y-\omega_i t+\theta_i \tag{2}$$

corresponding to the electrostatic field $\mathbf{E}=-\nabla\Phi$. The two wave vectors $\mathbf{k}_1$ and $\mathbf{k}_2$ are assumed to be nonparallel.

A. Equations of motion

We consider the guiding-center motion of a charged particle in the presence of a constant magnetic field $\mathbf{B}$ in the third direction. The drift velocity of the guiding center is $\mathbf{u}=(c/B^2)\mathbf{E}\times\mathbf{B}$. The equation of motion can be written explicitly:

$$\begin{bmatrix}\dot{x}\\ \dot{y}\end{bmatrix}=\frac{c}{B}\begin{bmatrix}-\nabla_y\Phi\\ \nabla_x\Phi\end{bmatrix}=\frac{c}{B}\sum_{i=1}^{3} a_i\begin{bmatrix}-k_i^y\\ k_i^x\end{bmatrix}\cos\xi_i(x,y,t)\ . \tag{3}$$

It can be shown that these equations of motion derive from an Hamiltonian $\mathcal{H}(x,y,t)=(c/B)\Phi(x,y,t)$ in which the coordinates (x,y) are canonical conjugate coordinates.

First of all we note that the explicit time dependence of two phases can be eliminated by writing the phases $\xi_i=\mathbf{k}_i\cdot\mathbf{r}-\omega_i t+\theta_i$ in a reference frame moving with a constant velocity $\mathbf{v}$:

$$\mathbf{r}'\equiv\mathbf{r}-\mathbf{v}t\ . \tag{4}$$

This velocity $\mathbf{v}$ is chosen by the resonance condition with two arbitrary "first" waves:

$$\begin{aligned}\omega_1&=\mathbf{k}_1\cdot\mathbf{v}\\ \omega_2&=\mathbf{k}_2\cdot\mathbf{v}\ ,\end{aligned} \tag{5}$$

(taken for instance to be the dominant waves). The components (v_x,v_y) of the velocity $\mathbf{v}$ are thus given by

$$\begin{bmatrix}v_x\\ v_y\end{bmatrix}=\begin{bmatrix}k_1^x & k_1^y\\ k_2^x & k_2^y\end{bmatrix}^{-1}\begin{bmatrix}\omega_1\\ \omega_2\end{bmatrix}=\frac{1}{\delta}\begin{bmatrix}\omega_1 k_2^y-\omega_2 k_1^y\\ \omega_2 k_1^x-\omega_1 k_2^x\end{bmatrix}\ , \tag{6}$$

where δ is a measure of the vector product of the first two wave vectors $\mathbf{k}_1\times\mathbf{k}_2$:

$$\delta\equiv k_1^x k_2^y-k_1^y k_2^x\neq 0\ . \tag{7}$$

The potential Φ can thus be written as

$$\begin{aligned}\Phi=&a_1\sin(\mathbf{k}_1\cdot\mathbf{r}'+\theta_1)+a_2\sin(\mathbf{k}_2\cdot\mathbf{r}'+\theta_2)\\ &+a_3\sin(\mathbf{k}_3\cdot\mathbf{r}'-\gamma_D t+\theta_3)\end{aligned} \tag{8}$$

in terms of only one Doppler-shifted frequency

$$\gamma_D\equiv\omega_3-\mathbf{k}_3\cdot\mathbf{v}=\frac{\gamma}{\delta}\ , \tag{9}$$

given in terms of

$$\gamma\equiv\begin{vmatrix}k_1^x & k_1^y & \omega_1\\ k_2^x & k_2^y & \omega_2\\ k_3^x & k_3^y & \omega_3\end{vmatrix}\ . \tag{10}$$

In this reference frame, the potential (8) exhibits an explicit time dependence which is only due to the presence of the third perturbing wave: the two-wave problem is integrable. Let us notice that a nongeneric three-wave system exists, with wave vectors and frequencies such that $\gamma_D=0$, corresponding to a time-independent Hamiltonian, and is thus completely integrable. The physical explanation comes from the fact that, in this case, the referential velocity $\mathbf{v}$ is also resonant with the third phase velocity. In the general case, however, the time dependence cannot be eliminated and the motion is governed by an effective one-and-a-half degrees-of-freedom Hamiltonian.

Let us consider the two first wave phases ξ_1 and ξ_2 as two independent variables in the rest frame. Expressing x and y in terms of ξ_1, ξ_2, and t, normalizing the time to the frequency ω_1 of the first wave ($\tau\equiv\omega_1 t$) leads us to the following equations of motion:

$$\dot{\xi}_1=-1-e_2\cos\xi_2-e_3\beta'\cos\xi_3(\xi_1,\xi_2,\tau)\ , \tag{11}$$

$$\dot{\xi}_2=-\nu_2+e_1\cos\xi_1+e_3\alpha'\cos\xi_3(\xi_1,\xi_2,\tau)\ , \tag{12}$$

where the dot denotes a time derivative with respect to τ, and the third phase

$$\xi_3(\xi_1,\xi_2,\tau)\equiv\alpha'\xi_1+\beta'\xi_2+\gamma'\tau+\tilde{\theta} \tag{13}$$

is time dependent. In these equations the normalized amplitudes have been defined by

$$e_i\equiv\frac{c}{B}\frac{\delta}{\omega_1}a_i\ , \tag{14}$$

and the parameters are

$$\alpha'\equiv\alpha/\delta,\quad \beta'\equiv\beta/\delta,\quad \gamma'\equiv\gamma/\omega_1\delta=\gamma_D/\omega_1\ , \tag{15}$$

with the resulting phase

$$\tilde{\theta}\equiv-\alpha'\theta_1-\beta'\theta_2+\theta_3\ . \tag{16}$$

Here the parameters α and β are defined by the vector products

$$\alpha\equiv k_3^x k_2^y-k_3^y k_2^x\ , \tag{17}$$

$$\beta\equiv k_3^y k_1^x-k_3^x k_1^y\ , \tag{18}$$

and take into account the relative directions of the three wave vectors, in the following expression of the effective frequency:

$$\gamma/\omega_1 \equiv -\alpha - \nu_2\beta + \nu_3\delta \ , \tag{19}$$

with

$$\nu_i \equiv \omega_i/\omega_1 \ . \tag{20}$$

Equations (11) and (12) can be derived from the following Hamiltonian in which the variables ξ_1 and ξ_2 are canonically conjugated:

$$\mathcal{H}(\xi_1,\xi_2,\tau) = -\xi_2 + \nu_2\xi_1 - e_1\sin\xi_1 - e_2\sin\xi_2 - e_3\sin(\alpha'\xi_1 + \beta'\xi_2 + \gamma'\tau + \tilde{\theta}) \ . \tag{21}$$

Although the ξ_1 and ξ_2 variables play a symmetrical role in the expression of $\mathcal{H}$, Eqs. (11) and (12) lead to the choice of ξ_2 as a momentum variable, and the Hamiltonian equations of motion read

$$\frac{\partial\mathcal{H}}{\partial\xi_2} = \dot{\xi}_1 \ , \tag{22}$$

$$\frac{\partial\mathcal{H}}{\partial\xi_1} = -\dot{\xi}_2 \ . \tag{23}$$

It is possible to reduce the system of equations (11) and (12) to an equivalent system governed by a unique second-order differential equation in only one variable. We obtain in this way an exact closed equation for the transverse motion, appropriate for approximate analysis.

We consider here the special class of systems in which the orientations of the three wave vectors are such that $\alpha' = -\beta' \equiv -\lambda$ and $\nu_2 = 1$, hence $\gamma' = \nu_3$. The general class $\lambda = -1$ is solved numerically in Sec. III. A specific example of three wave vectors in this class is represented in Fig. 1. By introducing the variables $R = \xi_1 - \xi_2$ and $S = \xi_1 + \xi_2$, the equations of motion (11) and (12) read

$$\dot{S} = -2 + e_1\cos\left[\frac{S+R}{2}\right] - e_2\cos\left[\frac{S-R}{2}\right] - 2e_3\lambda\cos\xi_3 \ , \tag{24}$$

$$\dot{R} = -e_1\cos\left[\frac{S+R}{2}\right] - e_2\cos\left[\frac{S-R}{2}\right] \ , \tag{25}$$

where $\xi_3 = -\lambda R + \nu_3\tau + \tilde{\theta}$. Differentiating Eq. (25) with respect to time, using Eq. (24), and normalizing time τ to $\mu \equiv (e_1e_2)^{-1/2}$, we obtain the following differential equation for the variable R:

$$\ddot{R} = -\sin R \pm [\mu + e\lambda\cos(\lambda R - \nu t' - \tilde{\theta})] \times (a^2 + 2\cos R - \dot{R}^2)^{1/2} \ , \tag{26}$$

where the dot denotes differentiation with respect to $t' \equiv \tau/\mu$, and the constants are defined by $a^2 \equiv (e_1^2 + e_2^2)/e_1e_2$, $\epsilon \equiv e_3/\sqrt{e_1e_2}$, and $\nu \equiv \nu_3/\sqrt{e_1e_2}$.

The system (24) and (25) admits, in the case where $e_1 = e_2$, an exact particular solution given by $R = \pm\pi$, which corresponds to straight lines $\xi_2 = \xi_1 \pm \pi$ in phase space (see, for instance, Fig. 2).

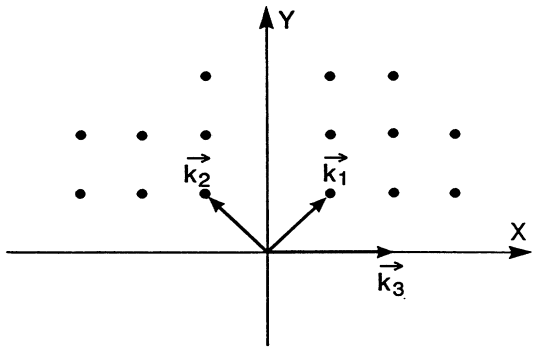

FIG. 1. Particular example of a three-wave configuration of the class $\alpha' = -\beta' = 1$.

The expression for the parallel component of the motion $S(t)$ (parallel to these straight lines in the case $e_1 = e_2$) can be expressed in terms of the solution of Eq. (26) for the transverse motion $R(t)$ as

$$S = 2\Theta(R) - 2\arccos\frac{R}{\mathcal{R}(R)} \ , \tag{27}$$

where $\dot{R}$ is the time derivative of the solution $R(t)$, and

$$\mathcal{R}(R) = \frac{1}{\mu}(a^2 + 2\cos R)^{1/2} \ , \tag{28}$$

$$\Theta(R) = -\arctan\left[\frac{e_1 - e_2}{e_1 + e_2}\tan\frac{R}{2}\right] \ . \tag{29}$$

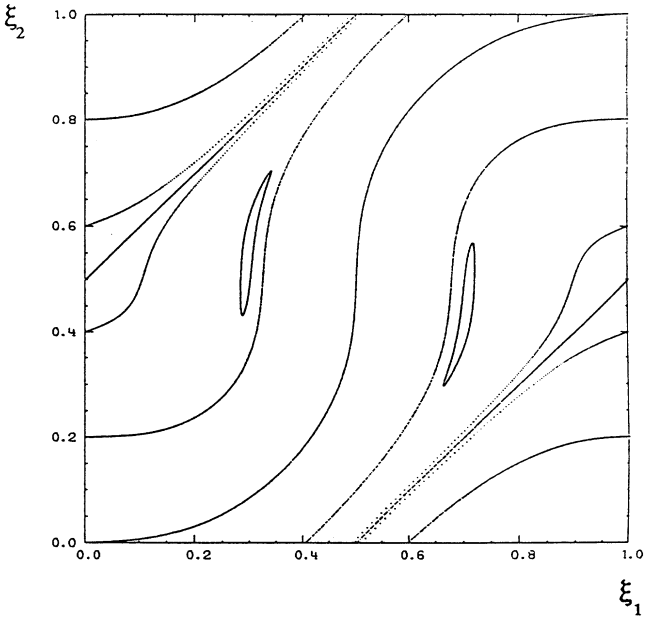

FIG. 2. Poincaré section over 1000 periods of nine trajectories with amplitudes $e_1 = e_2 = 0.9$ and $e_3 = 0.1$, and $\alpha' = -\beta' = 1$. Note the appearance of elliptic orbits. The initial conditions are ($\xi_1 = 0$, $\xi_2 = 0$), (0,0.5), (0.5,0), (0,0.8), (0,0.2), (0,0.4), (0,0.6), (0.3,0.5), and (0.7,0.5), modulo 2π

Of course, in the case where $e_3=0$, we recover an exact first integral of motion, which reads

$$a^2+2\cos R-\dot{R}^2=(\mathcal{E}_0-\mu R)^2 , \tag{30}$$

where $\mathcal{E}_0$ is a constant of integration, related to the unperturbed value $\mathcal{H}_0$ of the Hamiltonian by $\mathcal{E}_0=\mu\mathcal{H}_0$.

Except for the square-root factor and the constant μ in the square brackets, Eq. (26) has the form of the well-known equation governing the motion of a charged particle in two electrostatic waves (in the absence of magnetic field, in contrast with the present guiding center dynamics), to which a lot of theoretical and numerical works have been devoted [16]. Note that the latter equation can actually be obtained in the limit of infinite amplitude waves. Indeed in this limit $\mu\to 0$, and the invariant (30) reduces to the energy constant of the well-known nonlinear pendulum. Neglecting the μ term in the square brackets in Eq. (26), and replacing the square root by $\mathcal{E}_0$ [as follows from (30)], we get the announced result.

Since it has been shown extensively that the two-wave charged-particle problem exhibits chaos under certain conditions, this equivalence allows us to infer the following conclusion for our present problem of guiding centers in three waves: at least in the limit of infinite amplitude, the possibility of the existence of chaotic motion has been analytically predicted. Actually a chaotic solution also appears at weaker amplitudes, as will be numerically shown in Sec. III.

B. Perturbation of the analytical solution for the two-wave elliptic system

In the case of two electrostatic waves, the Hamiltonian (21), in which we set $e_3=0$, is obviously an exact invariant of motion, and therefore the motion is completely integrable. Two fundamentally different cases are found according to the values of the normalized amplitudes e_1 and e_2 with respect to ν_2 and 1, respectively.

1. Parametric solution

It is clear, from the equations of motion (11) and (12) with $e_3=0$, that no stationary singular point can exist if $e_2<1$, and $e_1<\nu_2$, which implies that no closed periodic orbits can exist, and therefore, no separatrix. Assuming these conditions to be fulfilled, it is possible to solve the equations of motion (11) and (12) in a parametric form. The Hamiltonian (21) (with $e_3=0$) appears as a generalization in two variables of the celebrated Kepler equation [20] of astronomy. Setting

$$\nu_2\xi_1-e_1\sin\xi_1=M , \tag{31}$$

we obtain a similar expression for ξ_2,

$$\xi_2+e_2\sin\xi_2=M-\mathcal{H}_0 , \tag{32}$$

where $\mathcal{H}_0$ is the constant value of the Hamiltonian (which is determined by the initial conditions). In the elliptic case $e_2<1$ and $e_1<\nu_2$ (i.e., elliptic motion in the Kepler equation), Eqs. (31) and (32) can be inverted univocally, and ξ_1 and ξ_2 can be exactly expressed as a convergent Fourier series with Bessel coefficients [20]:

$$\xi_1=\frac{M}{\nu_2}+\sum_{n=1}^{\infty}\frac{2}{n}J_n\left[\frac{ne_1}{\nu_2}\right]\sin\left[\frac{nM}{\nu_2}\right] , \tag{33}$$

$$\xi_2=M-\mathcal{H}_0+\sum_{s=1}^{\infty}(-1)^s\frac{2}{s}J_s(se_2)\sin[s(M-\mathcal{H}_0)] , \tag{34}$$

where M is a free parameter varying between $-\infty$ and $+\infty$. These results express the solution of the equations of motion in parametric form and represent the family of phase curves depending on the parameter $\mathcal{H}_0$. In order to get the time-law equation for these phase curves, we have to find an equation for the evolution of the parameter M with time. To this end, we differentiate Eqs. (33) and (34) with respect to time and get

$$\dot{\xi}_1=\frac{\dot{M}}{\nu_2}\left[1+\sum_{n=1}^{\infty}2J_n\left[\frac{ne_1}{\nu_2}\right]\cos\left[\frac{nM}{\nu_2}\right]\right] , \tag{35}$$

$$\dot{\xi}_2=\dot{M}\left[1+\sum_{s=1}^{\infty}(-1)^s2J_s(se_2)\cos[s(M-\mathcal{H}_0)]\right] . \tag{36}$$

From Eqs. (11), (12), and (31), we obtain $\dot{M}=-\dot{\xi}_1\dot{\xi}_2$, and thus

$$\dot{M}\left[1+\sum_{n=1}^{\infty}2J_n\left[\frac{ne_1}{\nu_2}\right]\cos\left[\frac{nM}{\nu_2}\right]\right]\times\left[1+\sum_{s=1}^{\infty}(-1)^s2J_s(se_2)\cos[s(M-\mathcal{H}_0)]\right]=-\nu_2 . \tag{37}$$

By expanding the product of the two series and integrating term by term with respect to time, we obtain time as a function of M and $\mathcal{H}_0$. As it is clear from the expressions for ξ_1 and ξ_2 as given by Eqs. (33) and (34), the motion is a periodic one if ν_2 is an integer, and we will only consider the case with equal frequencies ($\nu_2=1$). For this case we obtain

$$t_0-t=M(1+a_0)+\sum_{n=1}^{\infty}\frac{2}{n}\{J_n(ne_1)\sin(nM)+(-1)^nJ_n(ne_2)\sin[n(M-\mathcal{H}_0)]+(-1)^n\tfrac{1}{2}J_n(ne_1)J_n(ne_2)\sin(2nM-n\mathcal{H}_0)\}$$

$$+\sum_{n=1}^{\infty}\sum_{\substack{s=1\\ s\neq n}}^{\infty}2(-1)^sJ_n(ne_1)J_s(se_2)\left[\frac{\sin[(n+s)M-\mathcal{H}_0]}{n+s}+\frac{\sin[(s-n)M-s\mathcal{H}_0]}{s-n}\right] , \tag{38}$$

where t_0 is a constant of integration and

$$a_0(\mathcal{H}_0)=2\sum_{n=1}^{\infty}(-1)^n J_n(ne_1)J_n(ne_2)\cos(n\mathcal{H}_0)\ . \quad (39)$$

If M is incremented by 2π, the variables ξ_1 and ξ_2 increase by 2π and time by

$$T=-2\pi(1+a_0)\ , \quad (40)$$

and we deduce the frequency of the motion as

$$\omega(\mathcal{H}_0)=\frac{2\pi}{T}=\frac{-1}{1+a_0(\mathcal{H}_0)}\ . \quad (41)$$

For the particular case $\nu_2=1$, $e_2=e_1\equiv e<1$, and the particular values $\mathcal{H}_0=\pm\pi$, we find [20]

$$a_0(\mathcal{H}_0=\pm\pi)=2\sum_{n=1}^{\infty}(-1)^n J_n^2(ne)\cos(n\pi)$$
$$=(1-e^2)^{-1/2}-1\ , \quad (42)$$

hence a frequency

$$\omega_{e_1=e_2\equiv e}(\mathcal{H}_0=\pm\pi)=-(1-e^2)^{1/2}\ . \quad (43)$$

For the case $e_1<\nu_2$ and $e_2<1$ which has just been considered, in spite of the absence of singular points and especially of any saddle connection separatrix, the introduction of a small perturbation in the form of a third wave is expected to yield to a stochastic feature of the trajectories. Indeed, a representative example is given in Fig. 3, in which we draw the Poincaré section of six trajectories over 1000 periods corresponding to six uniformly spaced initially guiding center positions. In this example we have $e_1=e_2=0.9$ (hence the appearance of the straight lines $\xi_2=\xi_1\pm\pi$) with a perturbation $e_3=0.09$. As it is clearly seen in this figure, some surfaces in the phase space are destroyed. This result tends to corroborate the fact that, even if an unperturbed Hamiltonian (either linear as in Karney's case [21] or nonlinear as in the present case) does not have any singular point, the introduction of a nonlinear and resonant perturbation is able to make the system locally chaotic.

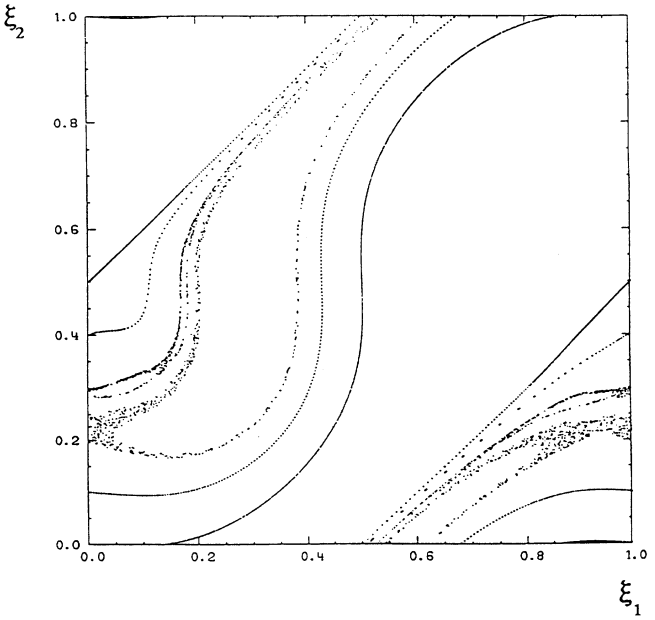

FIG. 3. Same as in Fig. 2, but with $e_3=0.09$ with initial conditions $\xi_1=0.0$, with six equally spaced values of ξ_2 ranging from 0 to 0.5.

2. *Angle-action variables*

It is clear that the motion of a particle in the present two-wave system is completely integrable. However, a simple exact analytical expression for the solution has been given, in Sec. II B 1 only for the case $e_1<1$, $e_2<1$. In this case, it is thus possible to investigate in an analytical approach the solution of the three-wave system, assuming that the normalized amplitude of the third wave is sufficiently small to be considered as a perturbation, and so to estimate the threshold for stochasticity in Sec. II B 3.

To this end, it is necessary to go over from the phase coordinates ξ_1 and ξ_2 to angle-action coordinates. In doing that, it is possible to deduce expressions for the angle, the action, the frequency of the motion, and the nonlinearity coefficient of the oscillator, along with the Fourier components of the perturbation corresponding to the different resonant terms involved in the expression for the threshold.

First, let us define as usual the action as

$$I(\mathcal{H}_0)=\frac{1}{2\pi}\oint\xi_2 d\xi_1\ , \quad (44)$$

where ξ_1 is the coordinate and ξ_2 the corresponding momentum. Using the expressions (33) and (34) (in which $\nu_2=1$), we get

$$I(\mathcal{H}_0)=\frac{1}{2\pi}\oint dM\left[1+\sum_{n=1}^{\infty}2J_n(ne_1)\cos(nM)\right]$$
$$\times\left[M-\mathcal{H}_0+\sum_{s=1}^{\infty}(-1)^s\frac{2}{s}J_s(se_2)\right.$$
$$\left.\times\sin[s(M-\mathcal{H}_0)]\right]\ . \quad (45)$$

Expanding the product of the series and integrating term by term, we obtain

$$I(\mathcal{H}_0)=\pi-\mathcal{H}_0-\sum_{n=1}^{\infty}(-1)^n 2\frac{J_n(ne_1)J_n(ne_2)}{n}\sin(n\mathcal{H}_0)\ , \quad (46)$$

from which we obtain the frequency

$$\omega(\mathcal{H}_0)\equiv d\mathcal{H}_0/dI=\frac{1}{dI/d\mathcal{H}_0} \quad (47)$$

in the form

$$\omega(\mathcal{H}_0)=\frac{-1}{1+\sum_{n=1}^{\infty}(-1)^n 2J_n(ne_1)J_n(ne_2)\cos(n\mathcal{H}_0)}\ , \tag{48}$$

which is identical to (41).

Knowing $I(\mathcal{H}_0)$ and $\omega(\mathcal{H}_0)$, we can calculate the nonlinearity coefficient of the oscillator, as given by

$$\Gamma(\mathcal{H}_0)=\frac{d\omega(\mathcal{H}_0)}{dI}=\frac{d^2\mathcal{H}_0}{dI^2}=\frac{d}{dI}\left[\frac{1}{dI/d\mathcal{H}_0}\right]$$
$$=-\omega^3(\mathcal{H}_0)\frac{d^2I}{d\mathcal{H}_0^2}\ , \tag{49}$$

where

$$\frac{d^2I}{d\mathcal{H}_0^2}=\sum_{n=1}^{\infty}(-1)^n 2nJ_n(ne_1)J_n(ne_2)\sin(n\mathcal{H}_0)\ . \tag{50}$$

It is important to notice that for trajectories with $\mathcal{H}_0=0$ or $\pm\pi$, we have $d^2I/d\mathcal{H}_0^2=0$ and thus $\Gamma=0$. For any value of e_1,e_2 the nonlinearity coefficient of this oscillator is vanishing; such trajectories will appear to correspond to the regions in phase space which, in the presence of the perturbation, give rise, for appropriate parameters values, to a thin stochastic zone extending in phase space, similar to a stochastic web [19].

For equal amplitudes of the two waves, the frequency $\omega(\mathcal{H}_0)$ given by (48) is even in $\mathcal{H}_0$, with a maximum on the straight line $\mathcal{H}_0=\pm\pi$ and a minimum on the S-shaped curve $\mathcal{H}_0=0$:

$$\omega_{e_1=e_2\equiv e}(\mathcal{H}_0=\pm\pi)=\frac{-1}{1+2\sum_{n=1}^{\infty}J_n^2(ne)}$$
$$=-(1-e^2)^{1/2}\ , \tag{51}$$

$$\omega_{e_1=e_2\equiv e}(\mathcal{H}_0=0)=\frac{-1}{1+2\sum_{n=1}^{\infty}(-1)^nJ_n^2(ne)}\ . \tag{52}$$

The frequency takes the particular values $\omega=-1/m$, with m an integer (i.e., "subharmonic" motion) on the straight line $\mathcal{H}_0=\pm\pi$ for the following values of the amplitude:

$$e_C(m)=(1-1/m^2)^{1/2}\ . \tag{53}$$

The curves $\omega(\mathcal{H}_0)$ are represented in Fig. 4 for $e=0.5$, 0.8, and 0.9. Due to the fact that the maximum frequency is localized on the straight line $\mathcal{H}_0=\pm\pi$, a phase curve having a frequency $\omega=-\frac{1}{2}$(i.e., a "subharmonic 2") will exist in the system provided that the amplitude is larger than the minimum threshold value: $e\geq e_C(2)=0.866$. Similarly, a curve with frequency $\omega=-\frac{1}{3}$ only appears at a value $e_C(3)=0.943$ of the amplitude e, and $\omega=-\frac{1}{4}$ at $e_C(4)=0.968$, etc.

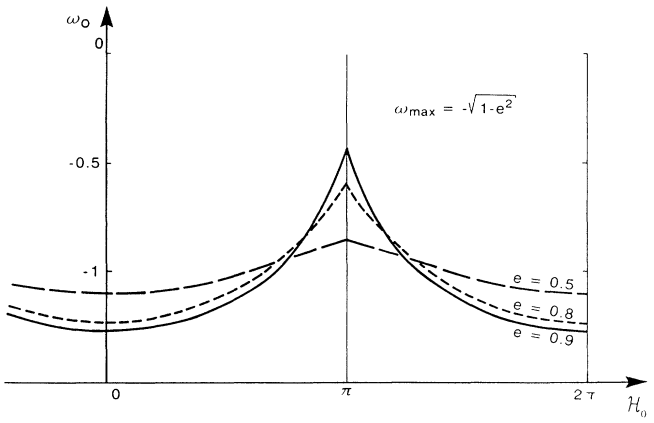

FIG. 4. Frequency in the two-wave system with equal amplitudes ($e_1=e_2\equiv e$) as function of the Hamiltonian $\mathcal{H}_0$, for $e=0.5$, 0.8, and 0.9. The critical values of the amplitude at which subharmonics appear are $e_C(m=2)=0.866$, $e_C(m=3)=0.943$, $e_C(m=4)=0.968$, $e_C(m=5)=0.980$, $e_C(m=6)=0.986$, and $e_C(m=7)=0.990$.

3. *Chirikov criterion*

We now consider the influence of the third perturbating wave, with $\lambda=-1$, $\nu_3=1$, and $\tilde{\theta}=0$, which yield $\mathcal{H}=\mathcal{H}_0+e_3\mathcal{H}_1$, with $\mathcal{H}_1=-\sin(\xi_1-\xi_2+\tau)$. By applying the standard Chirikov criterion for onset of stochasticity, we obtain the threshold value as [22]

$$s^2=\frac{32}{\omega^4}|e_3V_{m,n}\Gamma|_{I=I_{m,n}}\geq 1\ , \tag{54}$$

where $V_{m,n}$ is the Fourier amplitude of the perturbation corresponding to the resonance of order (m,n):

$$V_{m,n}=\frac{1}{(2\pi)^2}\int_0^{2\pi}d\Phi\int_0^{2\pi}d\tau\,\mathcal{H}_1(\Phi,I,t)e^{-i(m\Phi-n\tau)}\ . \tag{55}$$

The integration over τ shows that n is restricted to the values $n=\pm1$; we obtain

$$|V_{m,n}|=\frac{1}{4\pi}\int_0^{2\pi}d\Phi\,e^{-i[m\Phi-n(\xi_1-\xi_2)]}\ . \tag{56}$$

By the change of variables $\Phi\rightarrow M$, we express

$$d\Phi=\omega\,d\tau=-\omega(\mathcal{H}_0)dM\left[1+\sum_{n=1}^{\infty}2J_n(ne_1)\cos(nM)\right]$$
$$\times\left[1+\sum_{s=1}^{\infty}(-1)^s 2J_s(se_2)\cos[s(M-\mathcal{H}_0)]\right] \tag{57}$$

and

$$e^{\pm i(\xi_1-\xi_2)}\Longrightarrow e^{\pm i[\xi_1(M)-\xi_2(M)]}\ ,$$
$$e^{-im\Phi}\Longrightarrow e^{-im\omega(\mathcal{H}_0)[t(M)-t_0]}\ .$$

In principle, the problem is solved and the expression for $V_{m,n}$ is obtained by the evaluation of the integral on the

variable M. However, this integral seems very difficult to estimate, and we found it convenient to use another approach, which is presented in Sec. II D.

C. General features of the phase-space portrait with two waves

The above analytical solution (33), (34), and (38) of the equations of motion for the two-wave problem is restricted to "low" values of the amplitudes ($e_1 < \nu_2$ and $e_2 < 1$). The phase portrait in the general case can nevertheless be determined by the curves $\mathcal{H}_0(\xi_1,\xi_2)=$const [i.e., Eq. (21) with $e_3=0$]. Due to the secular combination $\xi_2-\nu_2\xi_1$, invariant curves are oriented mainly along the direction of the line $\xi_2=\nu_2\xi_1$ in phase space. From now on, we restrict ourselves for simplicity to the case of equal frequencies $\nu_2=1$ in which the unperturbed Hamiltonian reads

$$\mathcal{H}_0(\xi_1,\xi_2)=-\xi_2+\xi_1-e_1\sin\xi_1-e_2\sin\xi_2 \ . \tag{58}$$

In this case the phase portrait exhibits a spatial periodicity of 2π in each of the coordinates ξ_1 and ξ_2. In each cell of size 2π, invariant curves are periodically reproduced, with an increment of 2π for the corresponding value of $\mathcal{H}_0$ from cell to cell along the directions of the axis ξ_2 and $-\xi_1$.

An example is given in Fig. 5 for $e_1=e_2=0.9$ and in Fig. 6 for $e_1=e_2=1.2$, with ξ_1 and ξ_2 represented modulo 2π. In this simple case with equal values of e_1 and e_2, the straight lines $\xi_2=\xi_1+\pi\pm 2n\pi$ are obviously invariant curves corresponding to $\mathcal{H}_0=-\pi\pm 2n\pi$. Another remarkable invariant curve is the S-shaped curve $\mathcal{H}_0=0\pm 2m\pi$ passing through the center and the two opposite corners.

The salient feature in Figs. 6 and 7 (with $e_1>1$ and $e_2>1$) is the appearance of stationary points (elliptic or hyperbolic points), which obviously correspond to stationary phases of the waves, and thus to resonances of the guiding centers with these waves (x and y coordinates moving along straight lines with constant velocities). The generic phase portrait, corresponding to different values of the amplitudes, as given, for instance, by $e_1=1.2$ and $e_2=2$, is shown in Fig. 7, in which we see that the two hyperbolic points are not located on the same invariant curve.

From the equations of motion (11) and (12), the stationary points are found to be located at

$$\xi_1^0=\pm\arccos\left[\frac{\nu_2}{e_1}\right] \tag{59}$$

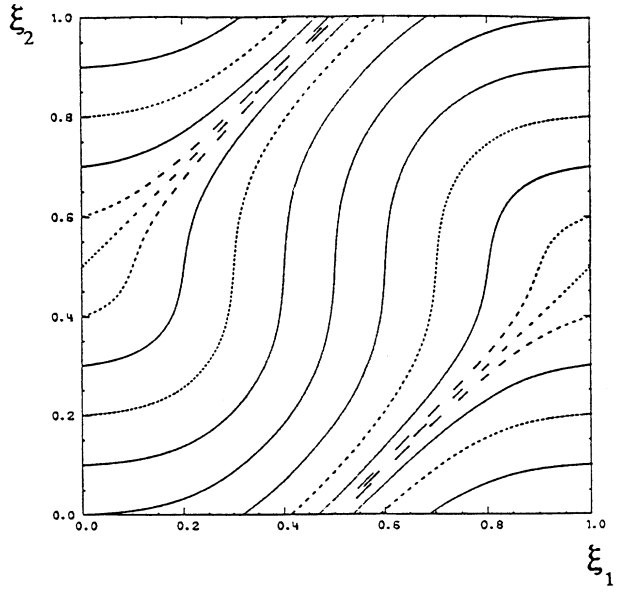

FIG. 5. Invariant curves $\mathcal{H}_0=$const for $\nu_2=1$, $e_1=e_2=0.9$, as a function of the two phases ξ_1 and ξ_2.

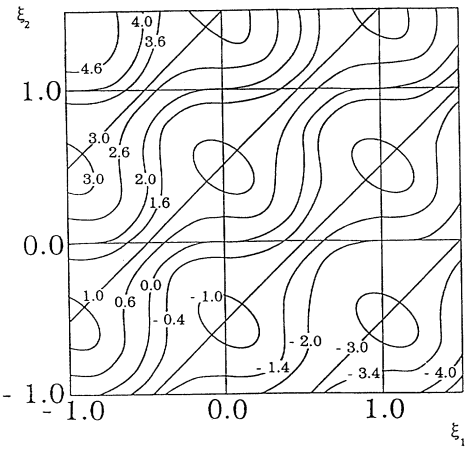

FIG. 6. Same as in Fig. 5, but with $e_1=e_2=1.2$, periodically reproduced in the unit cells. We note the existence of elliptic points, separatrices, with hyperbolic points aligned on the lines corresponding to odd values of $-\mathcal{H}_0/\pi$.

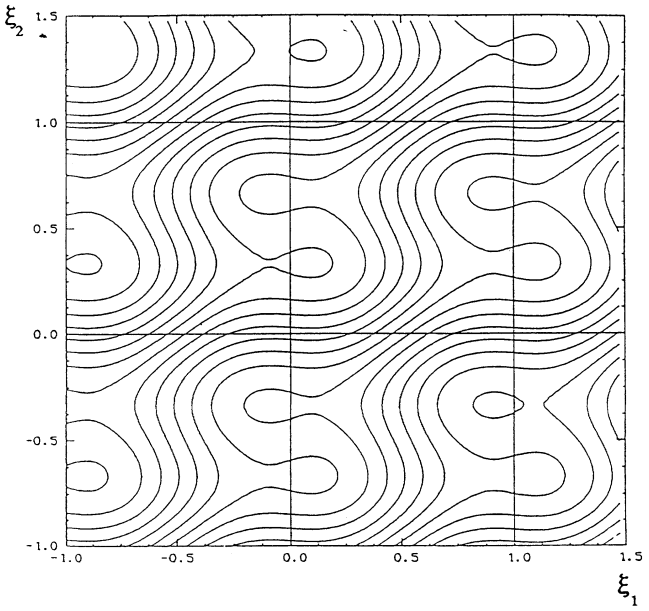

FIG. 7. Generic phase portrait representing invariant curves $\mathcal{H}_0/\pi=$const for $\nu_2=1$, $e_1=1.2$, and $e_2=2$. For different values of the amplitudes e_1 and e_2, we note the nonconnection of hyperbolic points.

and

$$\xi_2^0 = \pm \arccos\left[\frac{-1}{e_2}\right] . \tag{60}$$

The linear stability analysis performed around these four stationary points indicates the presence of elliptic or hyperbolic trajectories in the vicinity of these points, according to the sign of the quantity $e_1 e_2 \sin\xi_1^0 \sin\xi_2^0$ (positive or negative, respectively). Assuming $e_1, e_2 > 0$, we find the following values for the coordinates of the two elliptic points E_+ and E_-:

$$\xi_1^0(E_+) = b_1, \quad \xi_2^0(E_+) = \pi - b_2 ,$$
$$\xi_1^0(E_-) = -b_1, \quad \xi_2^0(E_-) = \pi + b_2 , \tag{61}$$

where $b_1 \equiv \arcsin[1-(1/e_1)^2]^{1/2}$ and $b_2 \equiv \arcsin[1-(1/e_2)^2]^{1/2}$. The values of the Hamiltonian (21) on the elliptic points are given by

$$\mathcal{H}_0(E_+) = -\pi + b_2 + b_1 - c_2 - c_1 ,$$
$$\mathcal{H}_0(E_-) = -2\pi - \mathcal{H}_0(E_+) ,$$

where $c_1 \equiv (e_1^2-1)^{1/2}$ and $c_2 \equiv (e_2^2-1)^{1/2}$.

Similarly, we find, for the two hyperbolic points H_+ and H_-,

$$\xi_1^0(H_+) = -b_1, \quad \xi_2^0(H_+) = \pi - b_2 ,$$
$$\xi_1^0(H_-) = b_1, \quad \xi_2^0(H_-) = \pi + b_2 , \tag{62}$$

with the corresponding values of the Hamiltonian

$$\mathcal{H}_0(H_+) = -\pi + b_2 - b_1 - c_2 + c_1 ,$$
$$\mathcal{H}_0(H_-) = -2\pi - \mathcal{H}_0(H_+) .$$

In the particular case of equal amplitudes ($e_1 = e_2$) we note that $\mathcal{H}_0(H_+) = \mathcal{H}_0(H_-) = -\pi$, which means that hyperbolic points are located in this case on the straight line $\xi_2 = \xi_1 + \pi$ (see Fig. 6). The phase portrait of this two-wave case is similar to the one obtained by Kleva and Drake [6] for their integrable "one-wave" system; their system represents the guiding-center motion in two plane waves in the particular case where $e_2 = -e_1$, $\omega_2 = -\omega_1$, $k_2^x = -k_1^x$ and $k_2^y = k_1^y$.

For large and equal amplitudes $e_1 = e_2$ we obtain merely confined trajectories in the space ξ_1, ξ_2, along with "rapid" trajectories making long jumps over several cells in each period: in Fig. 8 the invariant curves are almost confined in periodic squares. These squares correspond to the ones given previously for infinite amplitudes [6]. In the asymptotic case in which the amplitudes are infinitely large, the Hamiltonian can be reduced to the Hamiltonian describing a nonlinear pendulum constrained to oscillate in a plane rotating with a constant angular velocity about the vertical line (see, e.g., Ref. [23]).

D. Perturbation of the approximate solution in two plane waves

The difficulty of solving analytically in a closed form (not in a parametric form as previously done) the equations of motion for the two-wave system is essential and can be revealed by the fact that the integral on the variable R [Eq. (30)] cannot be found explicitly in terms of usual functions or even in terms of elliptic or hyperelliptic functions. As a consequence, the evaluation of the Fourier component $V_{m,n}$ of the resonant term (see Sec. II B 3) is also intractable. Thus, in order to give an estimate for the threshold, we have to resort to an approximate solution of the two-wave system.

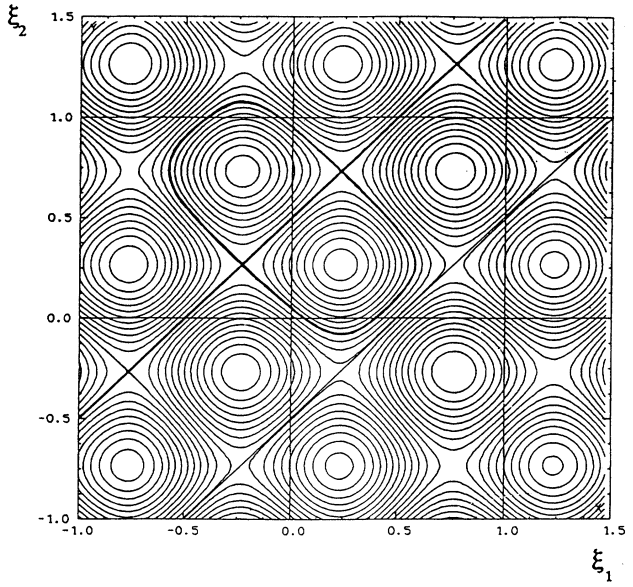

FIG. 8. Same as in Fig. 5, but for "large" amplitudes $e_1 = e_2 = 10$. We note pathways between trapped regions.

For $e_3 = 0$, the exact invariant of motion leads to the equation for R [use (30)]:

$$\left[\frac{dR}{d\tau}\right]^2 = e_1^2 + e_2^2 + 2e_1 e_2 \cos R - (\mathcal{H}_0 - R)^2 . \tag{63}$$

Now, the condition for the existence of solution in the real plane (R,τ) implies that $\mathcal{Y}_2(R) \equiv (\mathcal{H}_0 - R)^2$ should be less than $\mathcal{Y}_1(R) \equiv e_1^2 + e_2^2 + 2e_1 e_2 \cos R$, and thus R should be limited around the value of $\mathcal{H}_0$, due to the fact that $\mathcal{Y}_1(R)$ is bounded from below by $(e_1 - e_2)^2$ and from above by $(e_1 + e_2)^2$.

Drawing the sinusoidal curve $\mathcal{Y}_1(R)$ independent of $\mathcal{H}_0$ in Fig. 9, and the family of parabolas $\mathcal{Y}_2(R, \mathcal{H}_0)$ depending only on $\mathcal{H}_0$, we see that R is limited between the two values corresponding to the intersection points of the two curves (this corresponds to the finite amplitude of the oscillations observed in the trajectories in Fig. 5 for instance). This suggests that we make the change of variables $\rho = R - \mathcal{H}_0$ and consider ρ as a small quantity. Equation (63) becomes

$$\dot{\rho}^2 = e_1^2 + e_2^2 + 2e_1 e_2 \cos(\mathcal{H}_0 + \rho) - \rho^2 \tag{64}$$

and, approximating $\rho^2 \simeq 2(1-\cos\rho)$, the equation becomes the well-known equation of the nonlinear pendulum:

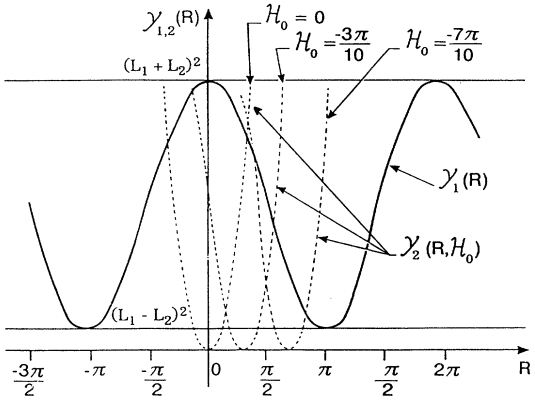

FIG. 9. The intersection of the sinusoidal curve $\mathcal{Y}_1(R)$ with the family of parabolas $\mathcal{Y}_2$ for the determination of the interval of variation of R around $\mathcal{H}_0$.

$$\dot{\rho}^2 \simeq -a_0^2 + b_0 \cos(\rho + \theta_0) , \tag{65}$$

with

$$a_0^2 = 2 - e_1^2 - e_2^2 ,$$

which is positive in the elliptic case, and

$$\theta_0 = \arctan \frac{e_1 e_2 \sin \mathcal{H}_0}{1 + e_1 e_2 \cos \mathcal{H}_0} ,$$

$$b_0^2 = 4(1 + e_1^2 e_2^2 + 2 e_1 e_2 \cos \mathcal{H}_0) .$$

The solution of Eq. (65) is given by

$$\rho = -\theta_0 + 2 \arcsin[\kappa \, \mathrm{sn}(s, \kappa)] , \tag{66}$$

where sn is the Jacobi elliptic function of argument κ, with

$$\kappa^2 = \frac{b_0 - a_0^2}{2 b_0} < 1 , \tag{67}$$

and the time is

$$s = \tau \sqrt{b_0/2} . \tag{68}$$

The inequality $\kappa^2 < 1$ is satisfied in the case $e_1 + e_2 < 2$.

It is now possible to express the Fourier component by putting in the perturbation term $\mathcal{H}_1$ of the Hamiltonian the approximate expression for R. We have

$$\mathcal{H}_1 = -\sin(\xi_1 - \xi_2 + \tau) = -\sin(R + \tau) \tag{69}$$

and we obtain an expression for the approximate value ω_{app} of the frequency of motion

$$\omega_{\mathrm{app}} = \omega^* \sqrt{b_0/2} , \tag{70}$$

where

$$\omega^* = \frac{\pi}{2K(\kappa)} \tag{71}$$

and $K(k)$ is the complete elliptic integral of first kind.

Together with the resonance condition

$$m\omega = \pm 1 ,$$

we have $\Phi = \omega(t - t_0)$, or $\Phi = \omega_{\mathrm{app}}(s - s_0)$, and we get

$$V_{m,n} = -\frac{\omega_0}{4\pi} \int_0^{4K} ds \, e^{-im\omega_0(s - s_0) + inR(\Phi, I)} , \tag{72}$$

where

$$e^{inR(\Phi, I)} = \exp(in\{\mathcal{H}_0 - \theta_0 + 2 \arcsin[\kappa \, \mathrm{sn}(s)]\})$$
$$= e^{in(\mathcal{H}_0 - \theta_0)} [\mathrm{dn}(s) + i n \kappa \, \mathrm{sn}(s)]^2 .$$

The integral (72) has been performed in Ref. [22], and we obtain

$$|V_{m,n}| = 2\omega_0^2 |m| e^{-|m\omega_0| K'(\kappa)} = 2|\omega_0| e^{-K'(\kappa)} . \tag{73}$$

Putting this last expression in the expression for the threshold as given by (54), we are in a position to compare this theoretical prediction for the onset of stochasticity due to overlapping of primary nonlinear resonances, with the numerical observations of stochastic motion in the same conditions (see Sec. VI A 5).

The comparison of the approximate frequencies calculated in this section with the exact ones is presented in Appendix A.

III. NUMERICAL STUDY OF THE ONSET OF CHAOS IN THE THREE-WAVE SYSTEM

In this section, we consider the same class of three-wave systems as in Sec. II B, with $\nu_3 = 1$ and with the specific values $\alpha' = -\beta' = 1$ (hence $\gamma' = 1$): a particular example of a three-wave-vector configuration is given in Fig. 1.

Numerical simulations have been performed to solve Eqs. (11) and (12) in this case, with arbitrary amplitudes, in order to study the influence of the third wave. We have restricted ourselves to the simple case with equal frequencies ($\nu_2 = \nu_3 = 1$) and the phase is taken to be $\tilde{\theta} = 0$. The equations of motion read

$$\dot{\xi}_1 = -1 - e_2 \cos\xi_2 + e_3 \cos(\xi_1 - \xi_2 + \tau) , \tag{74}$$

$$\dot{\xi}_2 = -1 + e_1 \cos\xi_1 + e_3 \cos(\xi_1 - \xi_2 + \tau) , \tag{75}$$

corresponding to $\lambda = -1$ in Eqs. (24) and (25). We have used a fourth-order Runge-Kutta integration algorithm, and checked the accuracy by verifying in the two-wave case the invariance of $\mathcal{H}_0$, as given in (58). The figures presented show the solutions of the equations of motion using the surface of section method (one point for each period, with ξ_1 and ξ_2 modulo 2π).

We should note a general symmetry that is apparent in these stroboscopic sections. The equations of motion [(58) and (59)] are actually invariant under the transformation

$$\xi_1' = 2\pi - \xi_1, \quad \xi_2' = 2\pi - \xi_2, \quad \tau' = -\tau . \tag{76}$$

This explains why the figures obtained for the stroboscopic sections are roughly unchanged by a rotation of π around the central point. [The slight difference that can, however, be observed in various figures between the right and left parts in the chaotic zones would disappear if we

had added characteristic points corresponding to negative values of time (backward trajectories).]

A. Perturbation of the "elliptic" case: $e_1, e_2 < 1$

First of all, let us consider the elliptic case with two equal amplitudes, i.e., $e_1 = e_2$ with $e < 1$, in order to determine the amplitudes of the third wave necessary to lead to local chaos and to large-scale stochastization of the trajectories (i.e., diffusion in the whole phase space).

1. Primary islands, the S-shaped curve, and the straight line

For a very low perturbation ($e_3 = 0.01$, $e = 0.9$) we observe in Fig. 2 a set of lines, which are followed in time by the stroboscopic position of the particle, toward increasing or decreasing values of ξ_1 and ξ_2. The effect of the perturbation can already be observed by the appearance of closed orbits corresponding to the existence of *primary resonances* ($m\omega = \pm 1$). More generally, we observe in this Fig. 2 a structure that appears to be generic for the case $e_1 = e_2$: the phase space (which is periodic in the two angles) appears to be divided in two areas well separated by two characteristic phase curves which are the most resistent to the perturbation:

(i) an S-shaped curve (corresponding to the unperturbed value $\mathcal{H}_0 = 0$) passing through the central point (0.5,0.5) and the corners (0.0,0.0) and (1.0,1.0); and

(ii) a straight line $\xi_2 = \xi_1 \pm 0.5$ (corresponding to the unperturbed value $\mathcal{H}_0 = \pm\pi$).

The motion along the straight line is analyzed in detail in a preliminary report [17] and can be described as follows. Introducing a relative and average phase variables $R = \xi_1 - \xi_2$, and $S = \xi_1 + \xi_2$ is equivalent to rotating the axis by an angle of $\pi/4$, S representing the coordinate which varies *along* the direction of the straight line. For equal values of the two first amplitudes, $e_1 = e_2 \equiv e$, the equations of motion are

$$\dot{S} = -2 - 2e \sin\frac{S}{2}\sin\frac{R}{2} + 2e_3 \cos(R + \tau) , \tag{77}$$

$$\dot{R} = -2e \cos\frac{S}{2}\cos\frac{R}{2} . \tag{78}$$

The straight line

$$\xi_2 = \xi_1 + \pi \tag{79}$$

corresponds to

$$R = -\pi , \tag{80}$$

and Eq. (78) ensures that this value is an exact invariant of the perturbed three-wave problem, whatever the value of the perturbation e_3. The straight line is thus an exact trajectory for $e_1 = e_2$, whatever the value of e_3.

The motion along the straight line is described by

$$\dot{\xi}_1 = -1 + e \cos\xi_1 - e_3 \cos\tau, \quad \xi_2 = \xi_1 + \pi . \tag{81}$$

One clearly sees from Eq. (81) that the velocity of a guiding center on the straight line vanishes when the following condition between the abscissa ξ_1^0 and the current time τ^0 is satisfied:

$$\cos\xi_1^0 = \frac{1 + e_3 \cos\tau^0}{e} . \tag{82}$$

These moving points on the straight line actually generalize the two hyperbolic points H_+ and H_- of the unperturbed two-wave system, which only appear for $e \geq 1$ (see Sec. IV):

$$\xi_1^0 = \pm\arccos\frac{1}{e} . \tag{83}$$

In the three-wave system, however, there do not exist fixed stationary points on the straight line, but only points of vanishing velocity: the particle stops, time increases, the condition (82) is no longer satisfied, and the particle starts again. This particular behavior observed in the simulations is explained by the formula (82).

By increasing the perturbation (Fig. 3 with $e_3 = 0.09$, $e = 0.9$), we observe an enhancement of the size of the two vortices located to the right and to the left of the central S-shaped curve; this causes a larger deformation of the S-shaped curve. In both parts of the phase space some lines are already destroyed, leading to thin *chaotic zones* localized around the separatrices. This structure, consisting in different chains of *large primary islands* located on both sides of the S-shaped curve (corresponding to $\mathcal{H}_0 = 2n\pi$), repeats itself in the full phase space.

By increasing further the perturbation ($e_3 = 0.2$ with $e = 0.9$ in Fig. 10), we observe the appearance of a pair of other primary islands (symmetrically repeated on both sides of the straight line). For this value of e, the resonance condition $m\omega_0 = \pm 1$, with integer values of m (see Sec. III), is indeed fulfilled for two and only two values of $\mathcal{H}_0$, corresponding to $\omega_0 = -1$ and -0.5, thus implying

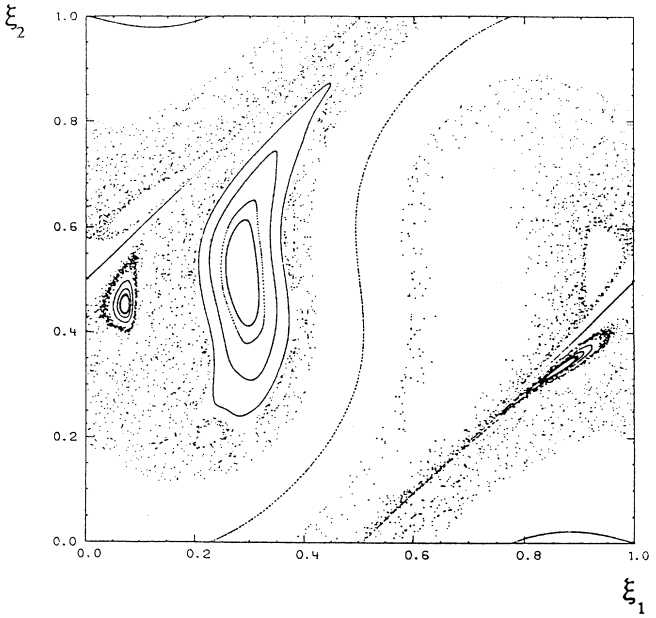

FIG. 10. Poincaré section over 1000 periods of 16 trajectories with $e_1 = e_2 = 0.9$ and $e_3 = 0.2$.

the existence of the two primary resonances seen in Fig. 10.

The number (m) of primary resonances is determined according to the value of e in the range

$$e_C(m) < e < e_C(m+1) , \tag{84}$$

where $e_C(m) \equiv (1-1/m^2)^{1/2}$ [see (53)]. For values of e approaching unity from below, the number of primary islands increases indefinitely: smaller and smaller islands appear in chains, with separatrices accumulating on both sides of the straight-line phase curve. For instance, for $e=0.96>e_C(3)$ and $e_3=0.05$, the stroboscopic section exhibits the different resonances $\omega=1$, $\frac{1}{2}$, and $\frac{1}{3}$.

Chains of *secondary islands* can be seen in the Fig. 10, close to the separatrix of the main resonance $m=\pm 1$. We note that their size could be larger than the size of primary islands corresponding to large values of m when e is close to unity.

For a perturbation $e_3=0.45$ (with the amplitude $e=0.9$), the chaotic zones become very large [Fig. 11(a)], with an increased size of the secondary islands. We note that the straight lines and the S-shaped curve are still resistant, along with other nearby trajectories, forming "pathways."

For a perturbation $e_3=0.81$, the chaotic sea is very large [Fig. 11(b) with $e=0.9$], but *remains confined* at some distance from the straight lines and from the S-shaped curve which still correspond to regular motion (the thin lines in the figures). The separatrix can be recognized by a small chaotic zone around the hyperbolic point ($\xi_1 \sim 0.05$, $\xi_2 \sim 0.65$). The motion along this chaotic zone allows a particle to diffuse in the direction S parallel to the straight line, but does not allow crossing this line: there is no diffusion in the perpendicular direction R.

Beside the primary islands and their destroyed separatrix, we see in Fig. 12, for $e=0.7$ (i.e., $m=1$), several chains of secondary islands, along with their own destroyed separatrices.

2. *Two hyperbolic points and the separatrices*

With a low value of e ($e=0.2$) stochastization is very weak and the numerical simulation of particle dynamics allows us to draw thin curves, even close to a hyperbolic point and so for relatively high values of the perturbation. Figure 13 ($e_3=0.18$) represents the typical situation corresponding to values $e_3 < e < 1$, with four fundamental curves characteristic of the structure of the phase space: the straight line, the S-shaped curve, and the two separatrices.

Around the straight line and the S-shaped curve, limited phase areas filled with nonclosed phase curves constitute pathways in which particles circulate. These pathways are confined by the separatrices and become tangent in two hyperbolic points. We note that trajectories cannot cross the straight line and are confined in the R direction.

For increasing values of the perturbation e_3, the S-shaped curve deforms itself, with more pronounced maxima and minima. We observe an important phenomenon: two hyperbolic points, which remain between the S-shaped curve and the straight line, come closer and closer to each other and finally collapse on the point (0,0.5) when $e_3=e$. Figure 14 represents different periodic cells, in order to illustrate the exact structure of the curves around the point (0,0.5). At this threshold value of the perturbation ($e_3=0.2$), the point (0,0.5) is actually a *double hyperbolic point,* connecting the straight line and the S-shaped curve. In the case of low amplitudes $e<1$, we will see that this seems to be the mechanism allowing a connection between different cells to be built and allowing a chaotic diffusion in the R direction perpendicular to the straight line.

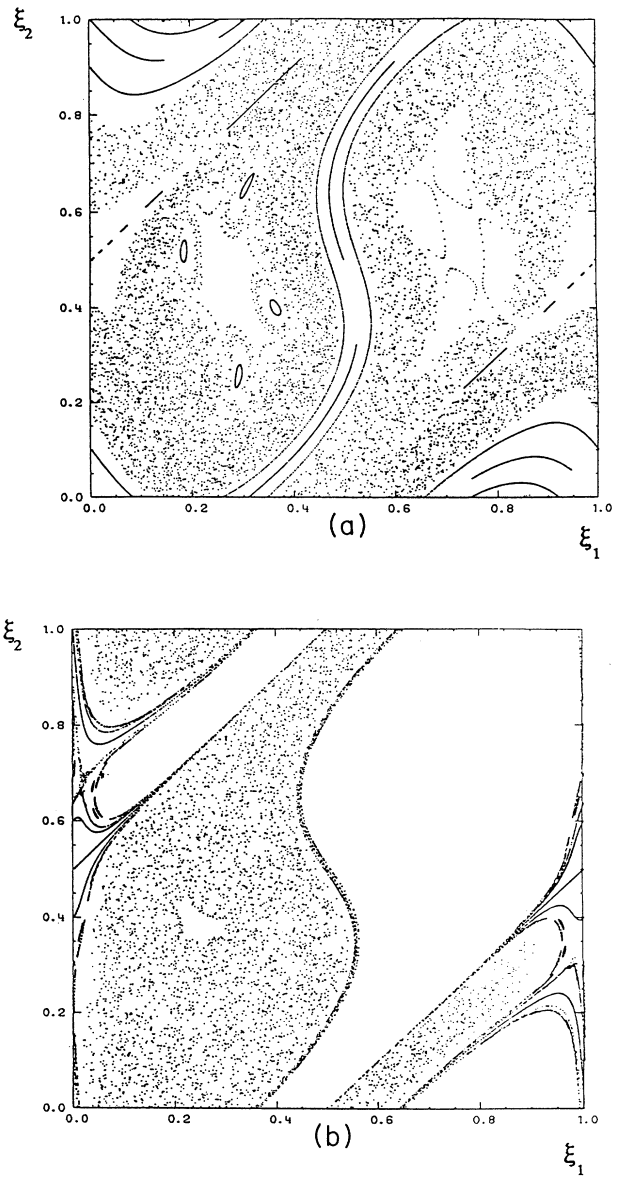

FIG. 11. (a) Poincaré section over 1000 periods of 14 trajectories with $e_1=e_2=0.9$ and $e_3=0.45$. There are 10 equally spaced initial conditions on the axis $\xi_1=0$, and 4 initial conditions on $\xi_1=0.3$ at $\xi_2=0.6$, 0.63, 0.65, and 0.7. (b) Same as in (a), but with $e_1=e_2=0.9$ and $e_3=0.81$.

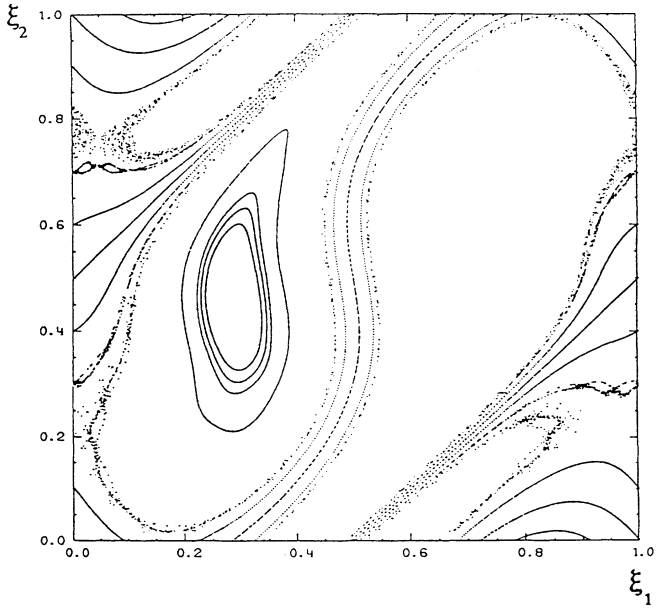

FIG. 12. Same as in Fig. 11(a), but with $e_1=e_2=0.7$ and $e_3=0.35$.

3. *Analytical description of the double hyperbolic point at the threshold $e_3=e<1$ in the elliptic case*

In terms of the variables

$$u=\xi_1+\tau, \quad w=\xi_1-\xi_2+\pi \ , \tag{85}$$

the equations of motion (74) and (75) can be written in the symmetrical form

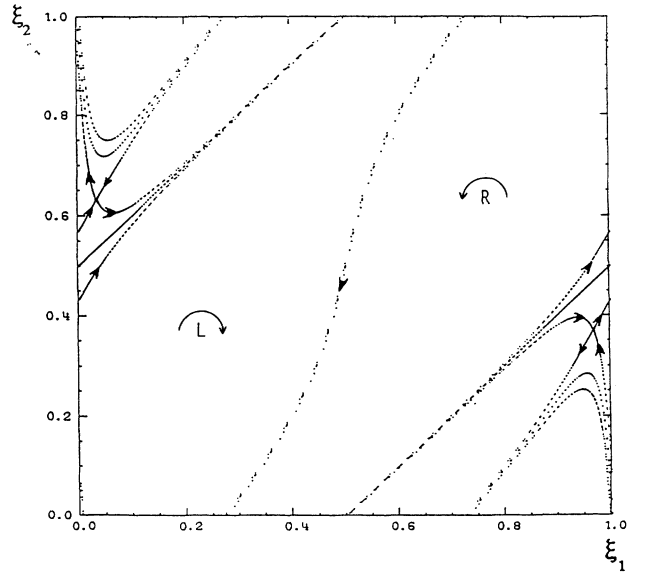

FIG. 13. Poincaré section over 1000 periods of 5 trajectories with $e_1=e_2=0.2$ and $e_3=0.18$. The vortices obtained in the left- and right-hand sides of the periodic cell are indicated by letters "*L*" and "*R*", respectively.

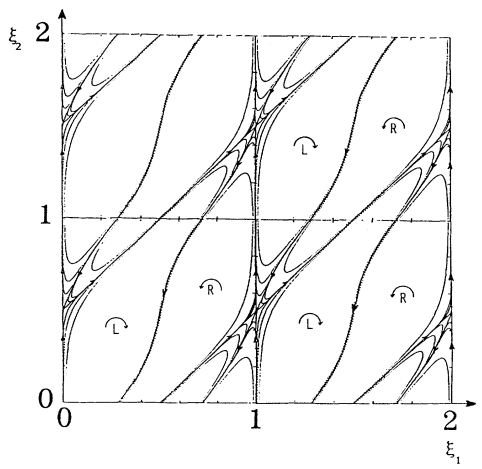

FIG. 14. Same as in Fig. 13, but with amplitudes $e_1=e_2=e_3=0.2$. The arrows along the separatrices indicate the collapse of the two hyperbolic points which were separated for lower values of e_3.

$$\dot{u}=e_2\cos[u-(w+\tau)]-e_3\cos(w+\tau) \ ,$$

$$\dot{w}=e_2\cos[(u-(w+\tau)]-e_1\cos(u-\tau) \ . \tag{86}$$

We clearly see the following: (i) for $e_3=e_2$ the quantity $u=2n\pi$ is invariant of the motion. In the phase space ξ_1,ξ_2 this means that the vertical sides of the periodic cell (see Fig. 14) are invariant of the stroboscopic section ($\tau=0,1,2$ times 2π). (ii) For $e_1=e_2$ the quantity $w=2m\pi$ is invariant of the motion. In the phase space ξ_1,ξ_2, this means that the straight lines $\xi_2=\xi_1+\pi+2m\pi$ are invariant of the stroboscopic section. As a consequence, at the threshold $e_3=e\,(\equiv e_1=e_2)$, the points

$$u=2n\pi, \quad w=2m\pi \tag{87}$$

correspond to *fixed points in the stroboscopic section* (0,0.5):

$$\xi_1=-\tau+2n\pi, \quad \xi_2=\xi_1+\pi+2m\pi \ , \tag{88}$$

i.e., a point of *periodically incremented phase* on the straight line: during each period, ξ_1 and ξ_2 are decreased by 2π. Physically this periodically incremented phase point, however, corresponds to a stationary point in the physical space. [The conservation of $u=0$ means indeed $\mathbf{k}_1\cdot\mathbf{r}=0$, i.e., the only particle motion is perpendicular to $\mathbf{k}_1$. On the other hand, the conservation of $w=0$ means $(\mathbf{k}_1-\mathbf{k}_2)\cdot\mathbf{r}=$const, i.e., that the only particle motion is perpendicular to $\mathbf{k}_3$. For a general wave-vector configuration in which $\mathbf{k}_1\cdot\mathbf{k}_3\neq 0$, we easily see that this forbids any motion in the plane. The physical meaning of the double hyperbolic point in (0,0.5) for $e_3=e$ thus *corresponds to a fixed point* $\mathbf{r}=$const in the physical space (x,y).]

As seen in Fig. 14, the straight line and the S-shaped curve are connected on this hyperbolic point. A simulation of the trajectory starting in the center of the S-shaped curve at the threshold $e_3=e$ indicates that the

point is approaching the hyperbolic point in time with a smaller and smaller velocity.

4. *Large perturbation $e_3 > e$: stochastic network and large-scale stochasticity*

For higher values of $e_3 > e$, we can see on Fig. 15(a) that the double hyperbolic point (the "crossing" between the straight line and the S-shaped curve) is split in both directions of larger and smaller values of ξ_1 ($e=0.6$, $e_3=0.8$). A more complete picture is given in Fig. 15(b) where we have repeated the unit cell. One can see that the S-shaped curve and the straight line become stochastized and go through these hyperbolic points. This thin chaotic zone actually forms an extended network which allows a trajectory to go over the entire phase space, but only on this restricted stochastic structure (analogous to a stochastic web [19]). It is important to note that this stochastic network is localized in the regions of degeneracy of the unperturbed system $\partial\omega_0/\partial\mathcal{H}_0=0$, which are indeed the S-shaped curve and the straight line. We note that in the present system a stochastic web with an infinite extension in phase space is obtained by perturbing a nonlinear Hamiltonian in its regions of degeneracy.

The whole importance of the collapse observed of the two hyperbolic points at the threshold value of the perturbation $e_3=e$ (as described in Sec. III A 2) consists in allowing the transformation of the stochastic zone of Fig. 11(b) into an infinite network in both directions S and R [Fig. 15(b)], i.e., in allowing two nonvanishing components of the asymptotic (tensorial) diffusion coefficient. We note that there still exist invariant curves, surrounding localized chaotic zones which remain confined around primary islands, thus with no asymptotic diffusion. The large-scale stochasticity is obtained only along the chaotic network.

Even for a perturbation $e_3=0.85$ with $e=0.6$, one trajectory fills a chaotic zone, which remains in one half-space. But on a longer period of time (4000 periods) Fig. 16 indicates that no clear separation persists between the two half spaces. *The threshold for large-scale stochasticity in the whole phase space seems to be reached* (for $e=0.6$) around a perturbation $e_3=0.85$, *beyond the collapse of the two hyperbolic points* at $e_3=e$. For a larger value of the amplitude ($e=0.8$), invariant curves still persist for a perturbation $e_3=0.9$: the threshold for large-scale stochasticity at an amplitude of $e=0.8$ is thus beyond $e_3>0.9$.

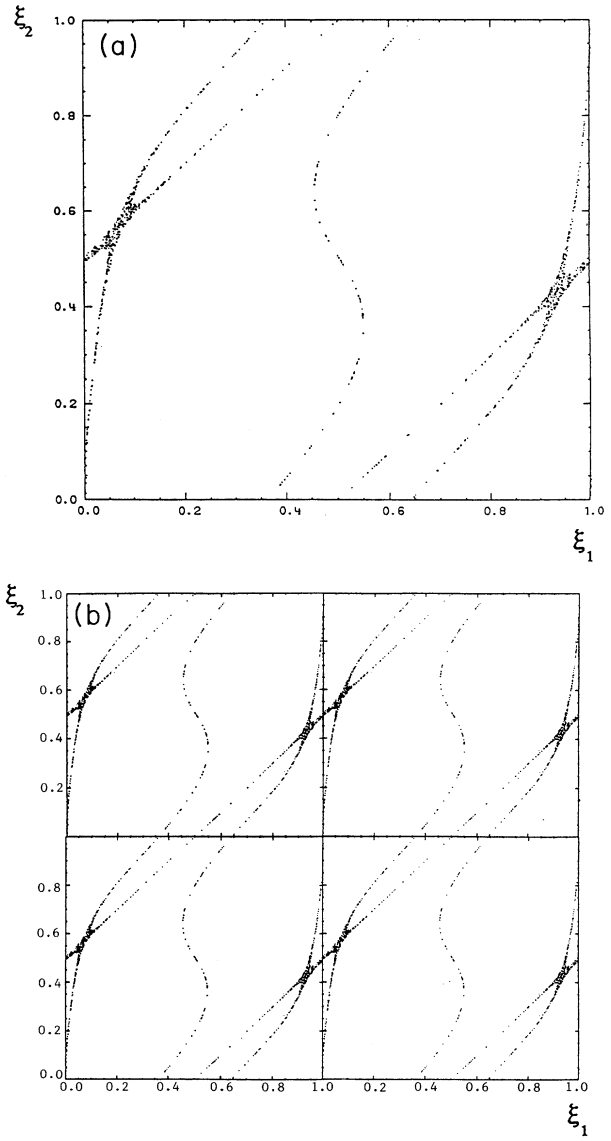

FIG. 15. (a) Poincaré section over 1000 periods of a single trajectory with $e_1=e_2=0.6$ and $e_3=0.8$. The initial condition is $\xi_1=0.25$, $\xi_2=0.75$, a point on the straight line $\xi_2=\xi_1+\frac{1}{2}\pm n$. Same as in (a) repeated over four unit cells, showing the spacial pattern of the stochastic web.

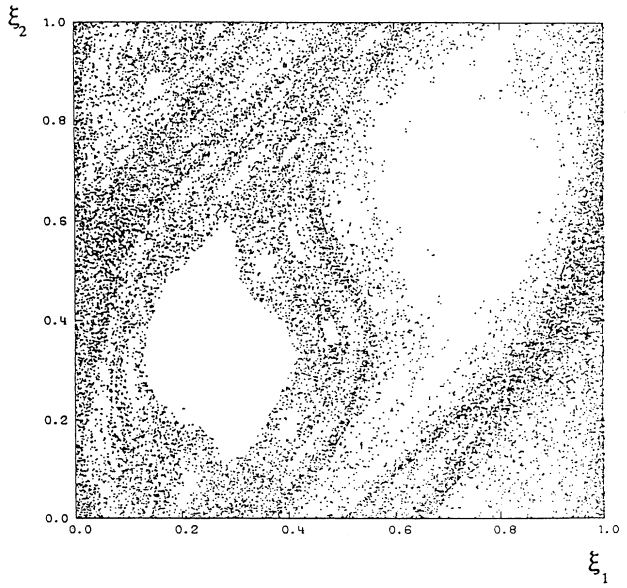

FIG. 16. Poincaré section over 4000 periods with $e_1=e_2=0.6$ and $e_3=0.85$ with five initial conditions. One (0.5,0.5) is on the central S-shaped curve, and four others in the different zones of Fig. 15 (a): (0.025,0.6), (0.975,0.4), (0.2,0.6), and (0.8,0.4).

For a larger value of the perturbation ($e=0.9$, $e_3=1$), Fig. 17(a) represents a solution starting from the straight line: the S-shaped curve still exists and is connected to the straight line by the chaotic zone. Even for a higher precision (1000 time steps per period), the chaotic zone exists and remains of finite width on the S-shaped curve. Starting on the S-shaped curve, however, and for a longer period of time, we observe that the characteristic point fills a large chaotic sea around the left vortex [Fig. 17(b) with 10 000 periods represented]. We conclude that, for the amplitude $e=0.9$, the threshold for filling the whole phase space (large-scale stochasticity) can only be reached with a larger perturbation of $e_3 \geq 1$.

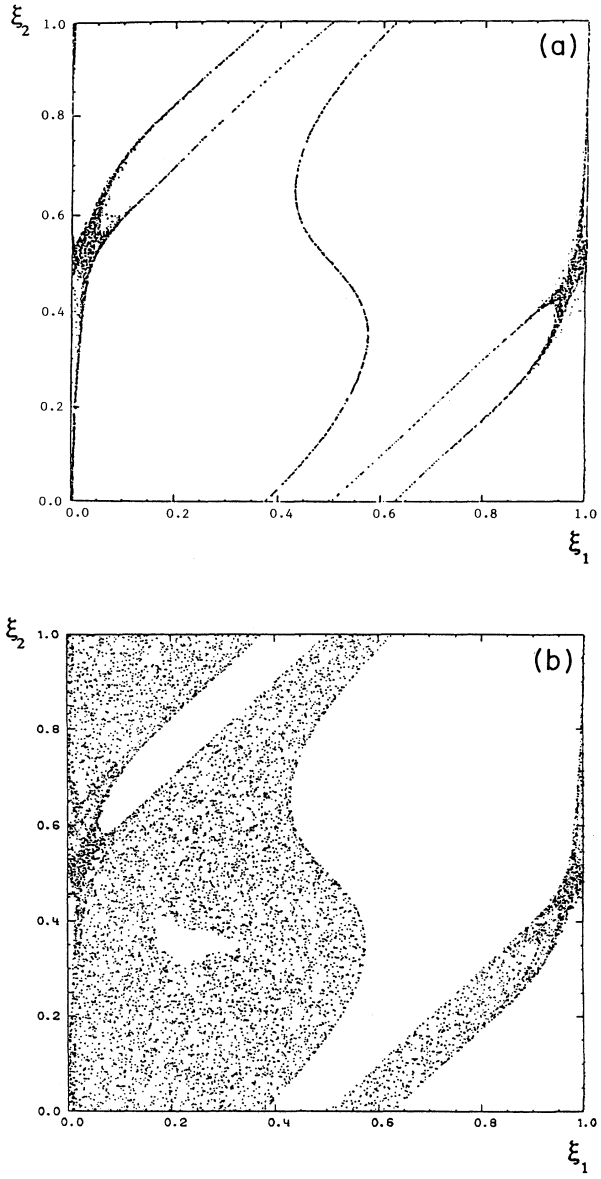

FIG. 17. (a) Poincaré section over 7000 periods with $e_1=e_2=0.9$ and $e_3=1.0$ of a single trajectory with initial condition (0.25,0.75) on the straight line $\xi_2=\xi_1+\frac{1}{2}\pm n$. (b) Poincaré section over 10 000 periods with $e_1=e_2=0.9$ and $e_3=1.0$ of a single trajectory with initial condition (0.5,0.5) on the central S-shaped curve.

5. *Theoretical values for resonance overlapping*

We analyze here different chaotic zones observed in the simulations, and compare the value of the perturbation e_3 with the analytical values deduced from preceding sections. Let us consider the large primary island in Fig. 12 corresponding to $m=1$ [$e=0.7<e_C(m=2)$]. This means that $\omega=\pm 1$ are the only primary islands in the system. The position of the fixed point can be evaluated to be roughly $\xi_1/2\pi=0.28$ and $\xi_2/2\pi=0.45$. For this point the unperturbed values of the Hamiltonian (58) and frequency (41) and (48) are $\mathcal{H}_0=-0.314$ and $\omega_0=-1.002$. For the island ($\omega\simeq -1$) the threshold for resonance overlapping as given by (54) is predicted to be

$$e_3(e=0.7;\omega\simeq -1)\geq 0.69 \ . \tag{89}$$

This value corresponds rather precisely to the collapse of the hyperbolic points, which occurs for $e_3=0.7$, as described in Secs. VI A 2 and VI A 3.

Another example can be taken in Fig. 10 [$e_3=0.2$, $e=0.9>e_C(m=2)$], corresponding to $m=2$. The fixed elliptic point of the primary resonance $\omega\sim -1$ can be evaluated to be roughly $\xi_1/2\pi=0.3$, $\xi_2/2\pi=0.55$. On this point we have $\mathcal{H}_0=-0.342$, $\omega_0=-1.012$. For this island ($\omega\sim -1$) the threshold is predicted to be

$$e_3(e=0.9;\omega\sim -1)\geq 0.362 \ . \tag{90}$$

This value is clearly much smaller than the value $e_3=0.9$ where the collapse of hyperbolic points occurs. This lowering of the threshold for $e=0.9$ can be understood from the appearance at this value of the amplitude e, of the other primary resonance $m=2$ ($\omega=\pm\frac{1}{2}$), and is due to the overlapping between $m=1$ and 2 modes. The predicted threshold gives an approximate value of e_3, which corresponds indeed to an intermediate case between Figs. 10 and 11(a), as expected.

On the other hand, if we search for the threshold of overlapping of the island $m=2$ in Fig. 10, we consider $\xi_1/2\pi=0.06$ and $\xi_2/2\pi=0.48$ and find $\mathcal{H}_0=-0.491$ and $\omega_0=-0.476$. The threshold obtained for this $m=2$ mode is found to be very low:

$$e_3(e=0.9;\omega\sim -\tfrac{1}{2})\geq 0.094 \ . \tag{91}$$

This can possibly be explained as due to the overlapping between $m=-\frac{1}{2}$ and $+\frac{1}{2}$ modes, which occurs even for very low amplitudes of the perturbation.

These results show that the values obtained from Eq. (53) for the threshold of resonance overlapping can be explained according to the number, nature, and sizes of the primary resonances present in the system for this value of the amplitude e. Of course, secondary islands can also be important [as seen in Figs. 10 and 11(a)] and could be responsible for overlapping between primary and secondary resonances of the same size. On the other hand, the threshold for large-scale stochasticity in the whole phase

space depends on more global processes like the destruction of the S-shaped curve, as discussed in Sec. III B.

B. Perturbation of the hyperbolic case $e_1, e_2 > 1$: breaking the S-shaped curve

By perturbing here also an equal-amplitude two-wave system, we ensure that the perturbation of the trajectory $\mathcal{H}_0 = \pm\pi$ remains a straight line. We note on Fig. 18 that the S-shaped curve still exists for $e=4$ with $e_3=2$. [The chaotic sea in the right part represents a single trajectory initiated on the straight line. This is not a numerical error: the straight line can easily be proved to be unstable in some specific points, at some specific times given by Eq. (82) (see Ref. [17]).] For $e_3=2.5$, the chaotic sea comes closer to the S-shaped curve which still exists. But for $e_3=2.80$ large-scale stochasticity is reached even when starting from the S-shaped curve: the S-shaped curve has thus been destroyed.

On Fig. 19(a) we observe an interesting phenomenon: for an intermediate value $e_3=2.65$ we observe an enlargement of the S-shaped curve in the region of low values of ξ_1. This enlargement is probably responsible for the filling of the left half-space at this value of the perturbation. A longer run would probably fill the whole space. In other words, for values of the perturbation e_3 around this transition value, the S-shaped curve has been replaced by a permeable structure. An enlarged picture of this region is represented on Fig. 19(b) for 2 particles initially located on the S-shaped curve: for a few hundred periods the characteristic point describes some structure around the S-shaped curve, but finally the point escapes into the chaotic sea.

A more detailed picture is drawn in Fig. 19(c) by taking 10 initial values on a line across this zone. Obviously the permeable structure replacing the S-shaped curve involves holes (islets) and sets of lines in this chaotic zone. This structure is probably the result (for an increasing value of the perturbation e_3) of the overlapping of secondary islets from both sides of the previous S-shaped curve.

We conclude that for this value of the amplitude $e=4$, the S-shaped curve is thus destroyed for a perturbation amplitude around $e_3=2.65$ and is replaced by a permeable structure which is *reminiscent of Cantori* [24], which usually results from the perturbation of KAM surfaces. This mechanism of transition toward large-scale stochasticity actually occurs at a value of the perturbation $e_3 < e$, i.e., before any collapse of hyperbolic points (as the one which has been found to occur in the elliptic case $e<1$ for a perturbation amplitude $e_3=e$).

We report in Appendix B the results of the simulations with different amplitudes for the two basic waves ($e_1 \neq e_2$). Although the straight-line trajectories are deformed in this case, the topology of the phase-space portrait is globally the same.

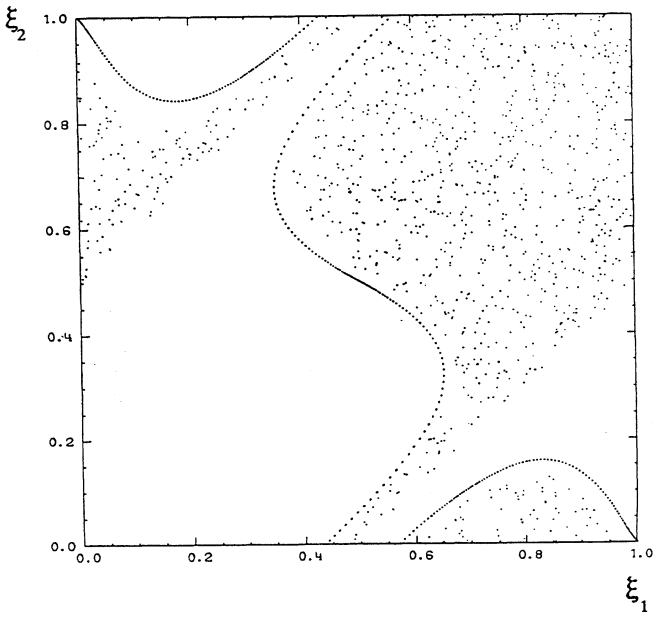

FIG. 18. Poincaré section over 1000 periods with $e_1=e_2=4.0$ and $e_3=2.0$ of two trajectories with initial conditions (0.5,0.5) on the S-shaped curve and (0.25,0.75) on the straight line.

C. Summary

The numerical simulations of the dynamics of guiding centers has allowed us to elucidate some mechanisms governing the appearance of chaos in the three-wave system, and to check some predictions of the analytical theory.

The general structure of the phase-space portrait with equal amplitudes of the first two waves ($e_1=e_2\equiv e$) is dominated by the existence of two oblique straight lines separated by a S-shaped curve. The motion of a guiding center along the straight line is observed to be in agreement with the analytical formulas (81,82).

In a typical case (Fig. 13) trapped trajectories are observed on each side of the S-shaped curve, with separatrices and hyperbolic points, and open trajectories are found along pathways on both sides of the straight lines.

Concerning the transition to large-scale diffusion in the three-wave system we reach the following conclusion. By perturbing an equal-amplitude two-wave system, we observe two different mechanisms leading to large-scale stochasticity.

(i) *For low amplitudes* (elliptic case: $e<1$) the perturbing wave is responsible for the appearance of elliptic points corresponding to fundamental modes $\omega=\pm 1$, located on both sides of the S-shaped curve. With higher and higher values of the amplitude e, other *primary island chains* appear in the form of subharmonics $\omega=\pm 1/m$ above threshold values $e_C(m)$ of the amplitude, in agreement with the analytic formula (53). The *localized chaotic zones* observed can be explained by the overlapping between such islands, which occurs for values of the perturbation amplitude e_3 which are in agreement with the prediction (54).

When the value of the perturbation e_3 reaches the

value e, the structure of the S-shaped curve becomes angular: *the two hyperbolic points collapse* on the straight line, allowing a direct connection with the S-shaped curve on a double hyperbolic point (Fig. 14), as predicted analytically in Sec. III A 3. Beyond this threshold, for $e_3 > e$, we observe a notable feature of the present three-wave system: the appearance of an extended *stochastic web* in the whole phase space, obtained by perturbation of a nonlinear system, but found only along the degeneracy regions (the straight line and the S-shaped curve).

The appearance of this stochastic network of chaotic trajectories is very important, as it allows *diffusion* in phase space. This process takes place not only inside localized chaotic zones (vanishing asymptotic diffusion), or

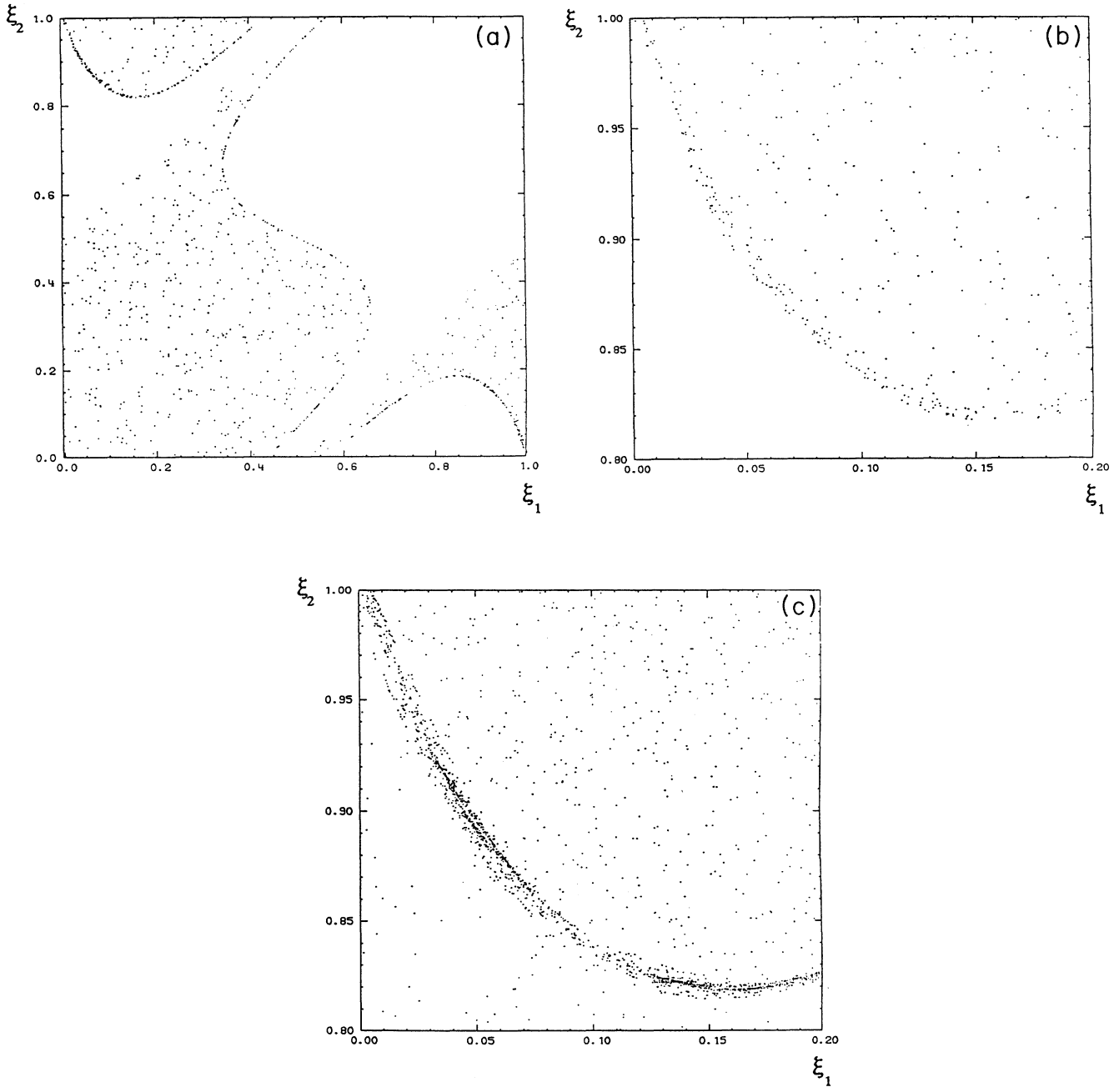

FIG. 19. (a) Poincaré section over 1000 periods with $e_1 = e_3 = 4.0$ and $e_3 = 2.65$ of a single trajectory with initial condition (0.5,0.5) on the S-shaped curve. (b) Part of the Poincaré section over 2000 periods with $e_1 = e_2 = 4.0$ and $e_3 = 2.65$ of two trajectories with initial conditions (0.0,0.0), (0.5,0.5) on the S-shaped curve. (c) Part of the Poincaré section over 1000 periods with $e_1 = e_2 = 4.0$ and $e_3 = 2.65$ of 16 trajectories with initial conditions $\xi_2 = 0.822$ and 16 equally spaced abscissa between 0.125 and 0.140 around the S-shaped curve.

along pathways parallel to the straight lines (anisotropic diffusion tensory with only parallel nonzero element), but also perpendicularly to these straight lines, i.e., in the whole phase space, yielding a nonvanishing asymptotic diffusion tensor.

(ii) *For higher amplitudes* ($e > 1$) we did not observe any stochastic web in the same sense. Large scale stochasticity is reached for a "lower" perturbation amplitude $e_3 < e$ at which the central S-shaped curve is replaced by a permeable structure, reminiscent of *Cantori.*

IV. CONCLUSIONS

The $\mathbf{E}\times\mathbf{B}$ guiding-center motion of particles in the field of two or three electrostatic waves propagating in a plane perpendicular to a uniform magnetic field has been investigated. We have shown that the motion in the case of two waves is completely integrable since the corresponding Hamiltonian has the form of a generalized Kepler equation, which can be solved exactly in the elliptic case.

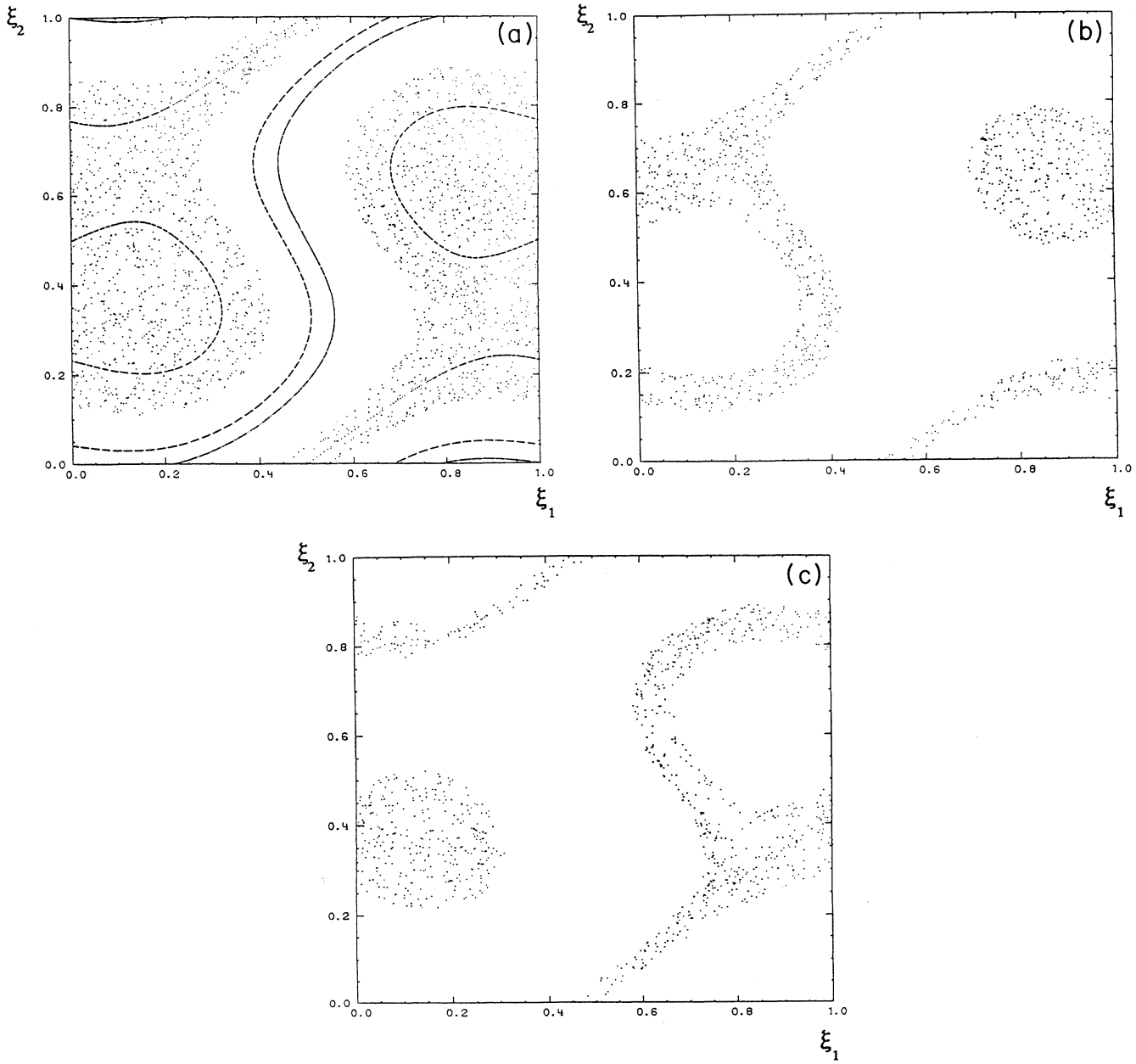

FIG. 20. (a) Poincaré section over 1000 periods with $e_1 = 1.2$, $e_2 = 2.0$, and $e_3 = 0.1$ of five trajectories with initial conditions: one on the S-shaped curve (0.5,0.5), the others at (0.0,0.5), (0.45,0.5), (0.0,0.68), and (0.0,0.32). (b) Poincaré section over 1000 periods with $e_1 = 1.2$, $e_2 = 2.0$, and $e_3 = 0.1$ of a single trajectory with initial conditions (0.0,0.68). The chaotic zone originates from the perturbation of the hyperbolic point H_+ of the two-wave problem. (c) Same as in (b), but with initial condition (0.0,0.4). The chaotic zone originates from the perturbation of the hyperbolic point H_- of the two-wave problem.

TABLE I. Precision of the approximate frequencies for $e_1=e_2=0.3$.

$\mathcal{H}_0/2\pi$	ω_0	ω_{app}	%
0.1 or 0.9	−1.035 542 14	−1.016 107 80	1.88%
0.2 or 0.8	−1.016 605 55	−1.000 341 02	1.60%
0.3 or 0.7	−0.989 906 97	−0.979 466 98	1.05%
0.4 or 0.6	−0.964 696 00	−0.961 256 03	0.36%
0.5	−0.953 939 04	−0.953 939 04	0.00%

In the hyperbolic case, corresponding to strong amplitude waves, an approximate solution (which reduces to the motion of a charged particle in two waves without magnetic field) has been deduced, from which an approximate determination of the threshold for onset of stochasticity can be derived in the presence of a third perturbing wave. In this simple system describing the onset of chaotic guiding center motion in three electrostatic plane waves, we have identified and checked numerically a variety of elementary processes (collapse of hyperbolic points, island overlapping, subharmonics, stochastic web, etc.) and threshold values predicted by the analytical treatment.

ACKNOWLEDGMENTS

We would like to thank Professor Radu Balescu from Association Euratom–Etat Belge in Brussels for his constant and stimulating interest in the present work. Mrs. Marie-Paule Valentin is also acknowledged for her technical assistance with the numerical tools. We also thank Professor Theo Geisel from Universität Würzburg and Professor Zaslawski and Professor Chernikov from the Moscow Institute of Space Research, for interesting discussions and suggestions on this problem. One of us (J.H.M.) also thanks cordially Professor Yves Elskens from the Université de Provence in Marseille for interesting and suggestive discussions about preliminary results.

APPENDIX A: COMPARISON OF THE APPROXIMATE FREQUENCIES WITH THE EXACT ONES

As shown in Table I the agreement between the approximate frequency [(70) and (71)] and the exact one [(41) and (48)] is rather good (deviation less than 2%) for a moderate value of the amplitude e. With a large value of the perturbation ($e_3=0.9$) the discrepancy may reach 20% not far from the straight line $\mathcal{H}_0=\pm\pi$, as shown in Table II.

TABLE II. Precision of the approximate frequencies for $e_1=e_2=0.9$.

$\mathcal{H}_0/2\pi$	ω_0	ω_{app}	%
0.1 or 0.9	−1.256 806 11	−1.138 983 10	9.37%
0.2 or 0.8	−1.195 155 36	−1.055 87284	11.65%
0.3 or 0.7	−1.081 049 43	−0.912 034 33	15.63%
0.4 or 0.6	−0.881 607 08	−0.693 296 09	21.36%
0.5	−0.436 538 82	−0.436 538 82	0.00%

APPENDIX B: GENERALIZATION OF THE RESISTANT STRAIGHT LINE FOR $e_1\neq e_2$

We also consider here the more general case of two basic waves with different amplitudes $e_1\neq e_2$ in which no straight-line trajectory can exist anymore. The topology, however, remains the same, and we see in Fig. 20(a) that

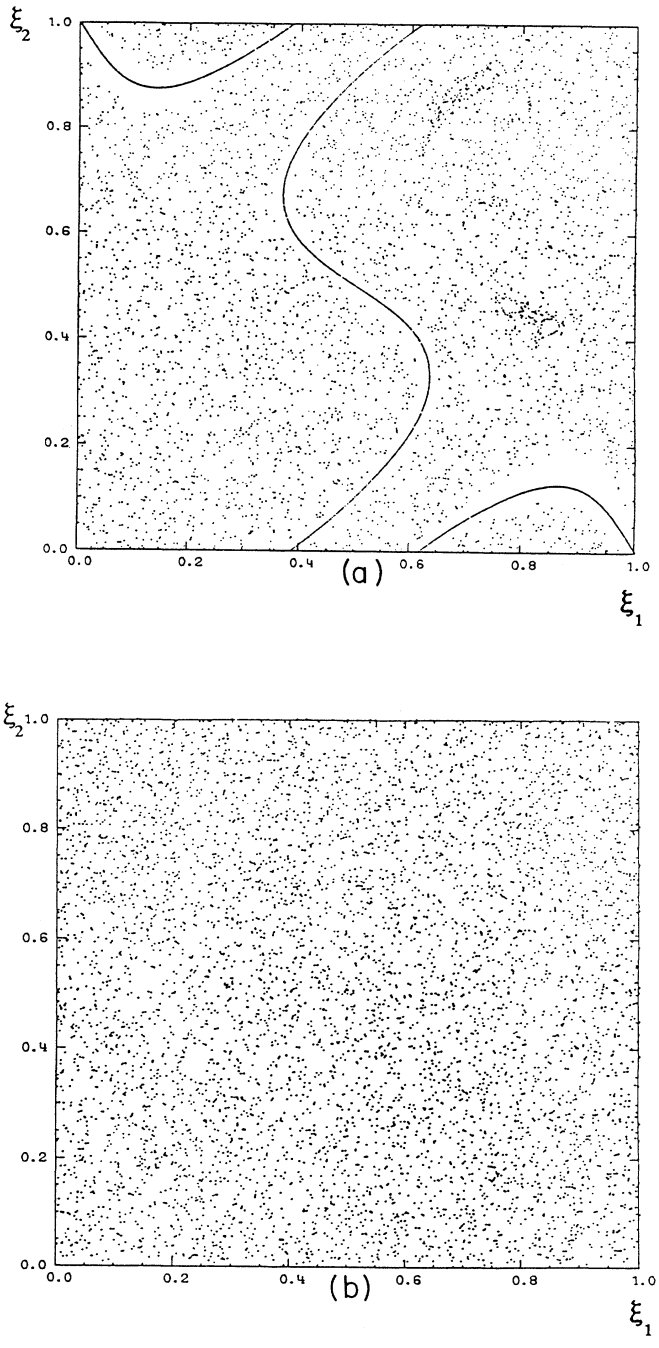

FIG. 21. (a) Same as in Fig. 20(a), but for a perturbation $e_3=1.0$. (b) Same as in Fig. 20(a), but for a perturbation $e_3=1.2$.

the straight line is actually replaced (for $\mathcal{H}_0=\pm\pi$, as in the unperturbed problem) by another curve which appears to be also resistant to the perturbation.

This curve can be seen to pass through $\xi_1=\frac{1}{2}$ and $\xi_2=\frac{1}{2}$ and to go down through two "bubbles." The chaotic zone inside the right bubble actually comes from the perturbation of the hyperbolic point H_+ of the unperturbed problem; this chaotic zone extends along the previous unperturbed separatrix [see Fig. 20(b) where the chaotic zone originated from the point $\xi_1=0$, $\xi_2=0.68$]. In a symmetric way, the left bubble corresponds to the unperturbed hyperbolic point H_- and extends along its separatrix [see in Fig. 20(c) where the chaotic zone originated from the point $\xi_1=0$, $\xi_2=0.32$].

We note that even a small perturbation $e_3=0.1$ in the case $e_1=1.2$, $e_2=2$ gives a large chaotic sea, approaching the generalization of the straight line. For a higher value of the perturbation $e_3=1$, this curve has been destroyed [see Fig. 21(a)] but the S-shaped curve is still resistent. Finally, for $e_3=1.2$, a full chaotic sea is obtained [Fig.. 21(b)]; the S-shaped curve has also been destroyed, probably by a mechanism involving a Cantori-like structure around the threshold, as observed in Fig. 19(c).

[1] W. Horton, *Handbook of Plasma Physics,* edited by A. A. Galeev and R. N. Sudan (North-Holland, Amsterdam, 1984), Vol. II.

[2] J. H. Misguich, R. Balescu, H. L. Pecseli, T. Mikkelsen, S. E. Larsen, and Qiu Xiaoming, Commisariat à l'Energie Atomique EUR-CEA-FC Report No. 1252, Centre d'Etudes Nucléaires de Caderache (France), 1985 (unpublished); Plasma Phys. Controlled Fusion 29, 825 (1987).

[3] T. H. Dupree, Phys. Fluids **10**, 1049 (1967).

[4] S. D. Hirshman and K. Molvig, Phys. Rev. Lett. **42**, 648 (1979).

[5] M. Pettini, A. Vulpiani, J. H. Misguich, M. De Leener, J. Orban, and R. Balescu, Phys. Rev. A **38**, 344 (1988).

[6] R. G. Kleva and J. F. Drake, Phys. Fluids **27**, 1686 (1984).

[7] W. Horton, Plasma Phys. **27**, 937 (1985).

[8] J. A. Robertson, Ph.D. dissertation, The University of Texas at Austin, 1986.

[9] T.F.R. Group and A. Truc, Plasma Phys. Controlled Fusion **26**, 1045 (1984).

[10] N. Fiedler-Ferrari, J. H. Misguich, and R. Balescu, Commisariat à l'Energie Atomique EUR-CEA-FC Report No. 1388, Centre d'Etudes Nucleáires de Caderache (France), 1990 (unpublished).

[11] M. De Leener, J. Orban, M. Pettini, A. Vulpiani, J. H. Misguich, and R. Balescu, in *Proceedings of the Congrès Société Française de Physique, Nice, 1985,* Bulletin de la Société Française de Physique No. 57 (Société Française de Physique, Paris, 1985), p. 56.

[12] M. De Leener, J. Orban, M. Pettini, and J. H. Misguich, in *Proceedings of the First European Fusion Theory Meeting, Wepion, 1986* (ULB, Bruxelles, 1986), p. 43.

[13] M. Pettini, A. Vulpiani, J. H. Misguich, R. Balescu, M. De Leener, and J. Orban, Commisariat à l'Energie Atomique EUR-CEA-FC Report No. 1271, Centre d'Etudes Nucleaires de Caderache (France), 1986 (unpublished).

[14] M. De Leener, J. H. Misguich, and R. Balescu (unpublished).

[15] J. H. Misguich, R. Balescu, and R. Nakach, in *Plasma Physics and Controlled Nuclear Fusion Research 1988,* Proceedings of the Twelfth International Conference on Plasma Physics and Controlled Nuclear Fusion Research, Nice, 1988 (IAEA, Vienna, 1989), p. 521.

[16] G. M. Zaslavskii and N. N. Filonenko, Zh. Eksp. Teor. Fiz. **54**, 1590 (1968) [Sov. Phys.—JETP **27**, 851 (1968)]; B. Rechester and T. H. Stix, Phys. Rev. Lett. **19**, 1656 (1979).

[17] R. Nakach and J. H. Misguich, Commisariat à l'Energie Atomique EUR-CEA-FC Report No. 1339, Centre d'Etudes Nucleaires de Caderache (France), (unpublished).

[18] T. Geisel (private communication).

[19] R. Z. Sagdeev, D. A. Usikov, and G. M. Zaslavsky, *Nonlinear Physics. From the Pendulum to Turbulence and Chaos* (Harwood Academic, New York, 1988).

[20] G. N. Watson, *A Treatise on the Theory of the Bessel Functions* (Cambridge University Press, Cambridge, England 1962), pp. 551 and 573.

[21] C.F.F. Karney, Phys. Fluids **21**, 1584 (1978).

[22] A. B. Rechester and T. Stix, Phys. Rev. A **19**, 1656 (1979).

[23] N. Minorsky, *Nonlinear Oscillations* (Krieger, Malabar, FL, 1962), p. 48.

[24] R. S. McKay, J. D. Meiss, and I. C. Percival, Phys. Rev. Lett. **52**, 697 (1984).